

BAYESIAN LEARNING OF MATERIAL DENSITY AND THE BLURRING FUNCTION, GIVEN 2-D IMAGES TAKEN WITH BULK MICROSCOPY TECHNIQUES

BY DALIA CHAKRABARTY^{*,||}, FABIO RIGAT^{†,††}, NARE GABRIELIAN^{‡,**,¶},
RICHARD BEANLAND^{§,||} AND SHASHI PAUL^{¶,**,¶}

, , , ,

*University of Warwick^{||}, De Montfort University^{**} Novartis Vaccines and
Diagnostics and University of Warwick^{††}*

We present a new non-destructive Bayesian inverse methodology to learn the unknown material density $\rho(\mathbf{x}) \geq 0$ and the unknown blurring function $\eta(z) \geq 0$, given 2-dimensional images of the material taken with the Scanning Electron Microscope (SEM), in Back Scattered Electrons or X-rays. Here \mathbf{X} is the 3-dimensional spatial vector, the third component of which is Z . The novelty of the advanced methodology lies in its ability to perform the estimation of the unknown functions via multiple (≥ 2), inversions, given that the image results from the projection of the convolution of unknowns, followed by spatial-averaging over a stipulated “interaction volume” inside the material, within which the electrons of the incident beam - during an electron scattering experiment - interact atomistically with the material. We expand the data space by invoking multiple images at distinct beam energies and invoke geometric priors on the density and strong priors on $\eta(z)$ using information available in existing microscopy literature. In our fully discretised model, the likelihood is defined as a function of the distance between the image data in a pixel and the contribution of the relevant voxels to the spatially-averaged projection of the convolution of the unknowns. The uniqueness of the estimates is discussed by viewing the posterior in the small noise limit. We also include the inversion of real SEM images of a blend of Nickel and Silver nanoparticles - with the aim of contributing towards increased understanding of lack of robustness of electrical characteristics of electronic devices made from such a nanostructure.

1. Introduction. Bulk electron microscopy involves the imaging of a material sample such that the image potentially carries information from its bulk, (as distinguished from images of thin films and foils), in a radiation that is generated as a result of the interaction between the molecular structure in the material and a beam of electrons that is imposed on it. The atomistic interactions give rise to a large variety of radiations when an electron beam is made incident on a given material sample. The capture of one such form of radiation, as a two dimensional image of the system, is possible with appropriate instrumentation such as a Scanning Electron Microscope (Goldstein, Newbury, Joy, Lyman, Echlin, Lifshin, Sawyer & Michael 2003; Lee 1993; Reed 2005). Here we focus on techniques that detect

^{*}Research fellow at Department of Statistics, University of Warwick; supported by a Warwick Centre for Analytical Sciences Research Fellowship

[†]Research Biostatistics Group Head, Novartis Vaccines and Diagnostics and Associate fellow at Department of Statistics, University of Warwick

[‡]Graduate student at Emerging Technologies Research Centre, De Montfort University

[§]Lecturer, Department of Physics, University of Warwick

[¶]Head, Emerging Technologies Research Centre, De Montfort University

Keywords and phrases: Bayesian inverse problems, Microscopy, Underdetermined problems

radiation emanating out of the bulk of the material sample after the atomistic interactions have taken place, upon the incidence of an electron beam on a cuboidal slab of the material sample.

Non-invasive and non-destructive 3-D density modelling of bulk material samples using 2-D images taken with electron microscopy techniques is often pursued in the hope of learning the structure of the material in its depth (Panaretos 2009) with the aim of controlling the experimental conditions under which material samples of desired qualities are grown (Davis et al. 2002). This is fundamentally a deconvolution problem since a two dimensional image - comprising an array of measured values of the radiation density per unit area - is inverted to estimate the (number or mass) density of the material that triggered the measured image in the first place, (Bertero & Boccacci 1998; Dorn, Bertete-Aguirre & Papanicolaou 2008; Natterer & Wbbeling 2001; Arridge & Schotland 2009). In practice, the situation is rendered more complicated by the fact that the radiation generated in three dimensions is modulated by processes inherent to the material sample. Thus, the projection of the convolution of the material density function with the material-dependent modulating (or blurring) function, into the space of the image, is averaged over the volume within which the atomistic interactions between the material and the incident electron beam stay confined, (Lee 1993; Goldstein et al. 2003). As for the modulation of the generated radiation, both enhancement and depletion of this are likely to occur. The nature of this modulation is then also of interest to the microscopist, in order to disentangle its effect from that of the unknown 3-D material density structure, that is responsible for generating the measured image. The simultaneous pursuit of both the unknown 3-D density and this material dependent, modulation or correction function, is less often addressed than are reported attempts at tomographic reconstruction, given the measured 2-D image and an assumed parametric model for the correction function, (Goldstein et al. 2003; Merlet. 1994; Heinrich & Newbury 1991; Pouchou & Pichoir 1984). These models suffer from lack of modularity in the dependence on unknown material-specific details and manifest questionable applicability in the case of inhomogeneous material samples. In particular, such reconstruction is difficult when the material density function is non-linear, non-convex and multimodal; this situation typifies real-life material samples, (Yamasaki et al. 2010; Park et al. 2010).

The projection of a density function $f(\mathbf{x})$ in a Hilbert space \mathcal{H} , $\mathbf{x} \in \mathbb{R}^n$, to the $n - 1$ -D image space \mathcal{D} , is referred to as the Radon Transform in n - see Helgason (1999), Kutchment (2006); here $n \in \mathbb{Z}^+$ and $f : \mathbb{R}^n \rightarrow \mathcal{H}$ is non-negative and real-valued. The inverse of the Radon Transform is also defined but involves the $n - 1 - th$ spatial derivative of $f(\mathbf{x})$, rendering the inverse Radon Transform an ill-conditioned problem if $f(\mathbf{x})$ is not Holder continuous or if the data comprises limited-angle images (Markoe & Quinto 1985; Rullgrd 2004) or if noise contaminates the data (Li & Speed 2000).

Learning the density from its projection is more often dealt with in the literature for $f \in \mathcal{G}$ where \mathcal{G} is a convex subset in \mathcal{H} . In the absence of measurements of the viewing angle, as Panaretos (2009) suggested, the implementation of Radon Transform is not directly possible. Even when the viewing angle is a measurable, the estimation of a non-convex $f(\mathbf{x})$ is difficult - this is dealt with in this paper; in

particular, we focus on the estimation of such a density that is also non-linear and multimodal, with the modes characterised by individualised, discontinuous sub-structure and abrupt bounds. Such modal shapes in general rule out the satisfactory implementation of a mixture model, while the blind implementation of the inverse Radon Transform (in 2-D) would not help, given the ill-conditioned nature of the problem. It appears therefore, that a pre-packaged transform is an unacceptably naive way forward and new methodologies need to be advanced towards the estimation of the unknown, non-linear, high dimensional functions. The methodology advanced herein is designed for applications to estimate material density using images taken by bulk electron microscopy techniques such as Scanning Electron Microscopy (SEM) that can image in the radiation of Back Scattered Electrons (BSE) or X-ray radiation¹. Given the nature of the unknown 3-D density as discussed above, we realise that the underlying distribution of the image data cannot be aptly modelled with a parametric form. Thus, a non-parametric model for the unknown density is motivated. In addition to the density, the method also provides an estimate of the unknown correction function - the discussion present in the current microscopy literature on the shape of the correction function (Merlet. 1994) is used to construct a semi-parametric model for the correction function that is sometimes implemented in the work while on other occasions, a nonparametric model for it is chosen.

We discuss the general inverse problem briefly in Section 2, followed by a brief discussion of the data. The model is discussed in details in Section 4, with Section 4.1 devoted to the geometric priors on the material density function while the following subsection discusses implementation of such priors in the model. Basic ideas about the correction function are introduced in Section 4.3 though the details have been relegated to Appendix A and B. The advanced inversion methodology is expounded upon in Section 4.4, with emphasis on the analysis of X-ray and BSE image data in Section 4.5 and 4.6 respectively. Inference is discussed in Section 4.7 with Section 4.8 and 4.9 involved with salient aspects of the uniqueness of the solutions. Application of the method to the analysis of real SEM image data is included in Section 5. Relevant aspects of the methodology are discussed in Section 6, with a summary presented in Section 7.

2. The general inverse problem. The general inverse problem is $I = \mathcal{P}(\rho) + \varepsilon$ where $I \in \mathcal{D}$ is data, while the unknown density $\rho \in \mathcal{H}$. If the mapping $\mathcal{P} : \mathcal{H} \rightarrow \mathcal{D}$ is the projection operator, then the dimensionality of \mathcal{D} is less than that of \mathcal{H} , leading to a fundamental ill-posedness (Tricomi 1985; Tarantola 2004). Also, ε is the measurement noise, the distribution of which, we assume known. In our application, the convolution of ρ and η , $\rho * \eta$, is mapped into \mathcal{D} by the projection operator \mathcal{P} .

A crucially higher level of complexity is introduced into the inverse problem relevant to this application in that $\mathcal{P}(\rho * \eta)$ requires to be spatially averaged over a known (from atomistic models) three dimensional region inside the material, with volume $V(E)$, $V \in \mathbb{R}$, $V > 0$ that depends on the energy E of the beam particles, $E \in \mathbb{R}$, given the material properties. This is the region, within which the interaction between the incident electron beam and the material molecules happens,

¹Imaging the near-superficial part of the sample in the radiation of the Secondary Electrons, is not included in our current discussion that is relevant to bulk microscopy data.

for a given beam incidence. This region is referred to as the ‘‘interaction-volume’’ in the microscopy literature. This 3-D region is centred at the point of beam incidence $(x_i, y_i, 0)$, $i = 1, \dots, N_{data}$ and its extent is determined by how energetic the electrons in the incident beam are. The spatial averaging, hereby represented by $\langle \cdot \rangle$, implies that the inverse problem we aim to work with is more difficult from usual since we estimate $\rho(\mathbf{x})$ and $\eta(\mathbf{x})$, from the data, where the measured 2-D radiation density, in the pixel centred at (x_i, y_i) , generated from the aforementioned atomistic interactions within the i -th interaction-volume, is:

$$(2.1) \quad I(x_i, y_i) = \langle \mathcal{P}(\rho * \eta) \rangle + \varepsilon \quad \text{or}$$

$$I(x_i, y_i) = \frac{\int_{R=0}^{R_{max}} \int_{\theta=0}^{\theta_{max}} R dR d\theta \int_{Z=0}^{Z=z_{max}(R, \theta)} \rho(\mathbf{x}) * \eta(\mathbf{x}) dz}{\int_{R=0}^{R_{max}} \int_{\theta=0}^{\theta_{max}} R dR d\theta} + \varepsilon$$

for $i = 1, \dots, N_{data}$. Here the spatial vector \mathbf{X} is given in the cylindrical coordinate system by the triple (R, θ, z) , with the transformations $x - x_i = R \cos \theta$, $y - y_i = R \sin \theta$ such that the interaction-volume is defined by radial coordinate $R \in [0, R_{max}]$, azimuthal coordinate $\theta \in [0, \theta_{max}]$, $Z \in [0, z_{max}]$ and the real-valued, non-negative bounds on the size of the interaction-volume are dependent on the beam energy E , with $z_{max} : \mathbb{R} \times \mathbb{R} \rightarrow \mathbb{R}$. Here, $\rho(\mathbf{x})$, $\mathbf{x} \in \mathbb{R}^3$, $\rho : \mathbb{R}^3 \rightarrow \mathbb{R}$, is the material density representing amount or mass of material per unit volume, $\rho(\mathbf{x}) \geq 0$. The measurements comprise the 2-D radiation density (eg. in backscattered electrons or X-rays) generated due to the beam pointings at discrete points $(x_i, y_i, 0)$ on the surface (surface is the $Z = 0$ plane) of the material where $i = 1, \dots, N_{data}$, i.e. the data comprise $\{\tilde{I}(x_i, y_i)\}_{i=1}^{N_{data}}$ measurements in N_{data} pixels.

3. Data. The data comprise a sequence of $N_{eng} \in \mathbb{Z}_+$ 2-D radiation density values recorded in a square spatial array of $N_{data} \in \mathbb{Z}_+$ number of pixels, $\{\tilde{I}_i^{(k)}\}_{k=1}^{N_{eng}}$, $i = 1, \dots, N_{data}$. In order to learn the density, using the measurements $\{\tilde{I}_i^{(k)}\}_{i=1}^{N_{data}}$ alone, we resort to the expansion of the information domain while creating the least number of logistical problems - we suggest imaging the system at multiple beam energies $\{\epsilon_k\}_{k=1}^{N_{eng}}$, where E is the real-valued discrete energy variable. For $E = \epsilon_k$, the image of the whole material sample is formed by N_{data} number of beam pointings on the surface of the material sample. For the k -th beam-energy ($E = \epsilon_k$), the measured 2-D discrete density, recorded due to the i -th beam pointing, is abbreviated as $\tilde{I}_i^{(k)}$, $\tilde{I}_i^{(k)} \in \mathbb{R}$, $\tilde{I}_i^{(k)} \geq 0$.

This aforementioned discrete nature of the beam pointings is a simplifying representation as compared to the continuous rastering of the beam on the material sample surface, during the SEM imaging. We will work with this artificial construct that the beam makes discrete pointings on the sample surface where the length scale characterising this discreteness is the resolution of the particular imaging technique at hand, given the microscope that is being used. Thus, the resolution is finer when the SEM image is taken in BSE ($\lesssim 0.01 \mu\text{m}$) than in X-rays ($\sim 1 \mu\text{m}$). Even finer spatial resolution in BSE images is possible with Field Emission Scanning Electron Microscopes (FESEM); see (Erlandsen, Macechko & Frethem 1999).

As discussed above in Section 1, noise in the data can crucially influence the stability of the solution of an inverse problem. Now, the data recorded with any

microscopy technique is subjected to noise, though very small; for example, in a typical 20s scan of the SEM, the signal to noise is about 200:1. Thus, for this scan of the SEM, the noise in the measurement of the 2-D BSE density - eg. $\tilde{I}_i^{(k)}$ in the k -th image - is $\sigma_i^{(k)} \approx 0.005\tilde{I}_i^{(k)}$, $k = 1, \dots, N_{eng}$, $i = 1, \dots, N_{data}$. In the following illustrations of our inversion methodology, the effect of the noise in the data is explored, even when noise is set to 10 times this value, at 5% of measured 2-D radiation density.

4. Model. We adopt a discrete model and the cuboidal material sample is put on a 3-D Cartesian grid with the sample surface $Z = 0$ such that the i -th beam-pointing is at the point $(x_i, y_i, 0)$. The gridding along the Z -axis is non-uniform, with the k -th bin including $Z = z \in [h_i^{(k-1)}, h_i^{(k)})$ where $h_i^{(k)}$ and $h_i^{(k-1)}$, are respectively, the electron stopping depths, given the k -th and $k - 1$ -th values of E , $k = 1, \dots, N_{eng}$. We define $h_i^{(0)} := 0$. The gridding along each of the X and Y -axes is set by the spatial resolution, δ , that the instrumentation can achieve. We learn the unknown functions $\{\rho(x_i, y_i, z_i^{(k)})\}_{k=1}^{N_{eng}}$ and $\{\eta(x_i, y_i, z_i^{(k)})\}_{k=1}^{N_{eng}}$, $\forall i = 1, \dots, N_{data}$. The interaction-volume formed at $E = \epsilon_k$ and the i -th beam-pointing, is referred to as the ik -th interaction-volume, for each $i = 1, \dots, N_{data}$ and each $k = 1, \dots, N_{eng}$.

It is known in the literature that the general, under-determined deconvolution problem is solvable only if the unknown density is intrinsically, ‘‘sufficiently’’ sparse (Donoho & Tanner 2005; Wright et al. 2009). Here we advance a methodology, within the frame of a designed experiment, to learn the density - sparse or dense. In the following subsection, we will see that geometric priors are more easily recognised if the density structure is sparse. With this in mind, the density is recognised to be made of low-rank $\rho_0(\mathbf{x})$ and sparse ($\rho_1(\mathbf{x})$) components. Thus, $\rho(\mathbf{x}) = \rho_0 + \rho_1(\mathbf{x})$, where ρ_0 is a constant (the low-rank component in the limiting sense), and $\rho_1(\mathbf{x})$ is the spatially varying component that may be sparse or dense. Then in our problem, for the k -th beam energy, the contribution of the low-rank part of the density to $\langle \mathcal{P}(\hat{\rho} * \hat{\eta}) \rangle$ is $\rho_0 \langle \mathcal{P}(\delta(\mathbf{x} - 0) * \hat{\eta}(\mathbf{x})) \rangle := I_0^{(k)}$, (for the k -th beam-energy) which is independent of the spatial location index if $\eta(\mathbf{x})$ is restricted to be a function of the depth coordinate only. This is indeed what we adopt in the model. $I_0^{(k)}$ depends only on the known morphological details of the interaction-volume for a beam of a given energy, for all beam incidence locations, $k = 1, \dots, N_{eng}$. Thus, the identification of the low-rank component of the density is easily performed as due to the low-rank component of a measurable, i.e. the image at a given k , where the image data at the k -th beam energy is $\{I_i^{(k)}\}_{i=1}^{N_{data}} = \{I_1^{(k)} + I_0^{(k)}\}_{i=1}^{N_{data}}$, where $I_1^{(k)}$ is the sparse/dense spatially-varying component of the image data. In our inversion exercise, it is the $\{I_1^{(k)}\}_{i=1}^{N_{data}}$ field that is actually implemented as data, after $I_0^{(k)} := \inf\{\tilde{I}_i^{(k)}\}_{i=1}^{N_{data}}$ is subtracted from $\{I_i^{(k)}\}_{i=1}^{N_{data}}$, for each $k = 1, \dots, N_{eng}$. Hereafter, when we refer to the data, the spatially dependent part of the data will be implied; this will now be referred to as $\{\tilde{I}_i^{(k)}\}_{i=1}^{N_{eng}}$, at each beam energy index $k = 1, \dots, N_{eng}$. Its inversion will yield a spatially varying (sparse/dense) density, that we will from now, be referred to as $\rho(\mathbf{x})$ that in general lies in a non-convex subset $\mathcal{G} \in \mathcal{H}$. Thus we see that in this model, it is possible for $\rho(\mathbf{x})$ to be 0. The construction of the full density, inclusive

of the low-rank and the estimate of spatially-varying parts, is straightforward once the latter estimate is obtained.

4.1. *Geometric priors.* In this section we discuss the possibility of availing of prior information on the density, that might be extracted by examining the geometrical aspects of the problem. In the Bayesian paradigm, the regularisation that is required to render the problem well-posed, is borne by the prior (Stuart 2010; Cotter, Dashti & Stuart 2010).

In our attempt to learn $\rho(\mathbf{x})$ and $\eta(\mathbf{x})$, given the image data, we identify the voxels in which $\rho(\mathbf{x}) = 0$. This identification will be made possible by invoking the nature of the operator $\langle \mathcal{P}(\cdot) \rangle$. For example, we realise that it is possible for the measured 2-D radiation $\tilde{I}_i^{(k)}$ collected from the ik -th interaction-volume to be non-zero, even when density in the ik -th voxel is zero, owing to contributions to $\tilde{I}_i^{(k)}$ from neighbouring voxels that are included within the interaction-volume over which the spatial averaging of $\mathcal{P}(\rho_i^{(k)} * \eta^{(k)})$ is performed. Such understanding is used within the forward problem, to identify the voxels in which density is zero. For a voxel that is not such, we subsequently learn the value of the density. The constraints that lead to the identification of voxels with null density can then be introduced into the model via the prior structure, in the following ways.

1. In the forward problem, we check if $\langle \mathcal{P}(\hat{\rho}(x_i, y_i, z_i^{(k)}) * \hat{\eta}) \rangle = \langle \mathcal{P}(\hat{\rho}(x_i, y_i, z_i^{(k)}) * \hat{\eta}) \rangle_{-mk}$, where $\langle \mathcal{P}(\cdot) \rangle_{-mk} :=$ spatial-averaging without including $\hat{\rho}(x_m, y_m, z_m^{(k)})$. If so, then we set $\hat{\rho}(x_m, y_m, z_m^{(k)}) = 0$.
2. In general, $\forall i = 1, \dots, N_{data}, k = 1, \dots, N_{eng}, \hat{\rho}(x_i, y_i, z_i^{(k)}) > 0 \implies \langle \mathcal{P}(\hat{\rho}(x_i, y_i, z_i^{(k)}) * \hat{\eta}) \rangle > \langle \mathcal{P}(\hat{\rho}(x_i, y_i, z_i^{(k-1)}) * \hat{\eta}) \rangle$. However,

$$(4.1) \quad \hat{\rho}(x_i, y_i, z_i^{(k)}) = 0 \implies \langle \mathcal{P}(\hat{\rho}(x_i, y_i, z_i^{(k)}) * \hat{\eta}) \rangle < \langle \mathcal{P}(\hat{\rho}(x_i, y_i, z_i^{(k-1)}) * \hat{\eta}) \rangle.$$

The inverse of statement 4.1 is also true, unless either one or both of the following two conditions are true - the discretisation scale is ‘‘sufficiently’’ coarse and/or if $\hat{\rho}(x_i, y_i, z_i^{(k)})$ is ‘‘sufficiently’’ low, where the aforementioned ‘‘sufficiency’’ can be quantified given the detailed geometry of the ‘‘interaction volume’’. The two caveats are seldom realised in practice, implying that the inverse of the statement 4.1 is likely. We model this, by first defining the random variable $\tau_i^{(k)} \in \mathbb{R}$ such that

$$\tau_i^{(k)} \stackrel{(4.2)}{=} \frac{\langle \mathcal{P}(\hat{\rho}(x_i, y_i, z_i^{(k)}) * \hat{\eta}) \rangle}{\langle \mathcal{P}(\hat{\rho}(x_i, y_i, z_i^{(k-1)}) * \hat{\eta}) \rangle}, \quad \text{for } \hat{\rho}(x_i, y_i, z_i^{(k-1)}) > 0,$$

$$\langle \mathcal{P}(\hat{\rho}(x_i, y_i, z_i^{(k)}) * \hat{\eta}) \rangle < \langle \mathcal{P}(\hat{\rho}(x_i, y_i, z_i^{(k-1)}) * \hat{\eta}) \rangle$$

$$\tau_i^{(k)} := 1 \quad \text{else}$$

for $i = 1, \dots, N_{data}, k = 1, \dots, N_{eng}$. Then the inverse of statement 4.1 is the same as the statement ‘‘ $\tau_i^{(k)} < 1$ implies that it is likely that $\hat{\rho}(x_i, y_i, z_i^{(k)}) = 0$ ’’. To build this constraint into the priors for $\rho(\mathbf{x})$, we define the probability density of $\tau_i^{(k)}$ as

$$(4.3) \quad \nu_i^{(k)}(\tau_i^{(k)}) = p^{\tau_i^{(k)}} (1-p)^{1-\tau_i^{(k)}},$$

where $\nu_i^{(k)}$ is a probability density and the hyperparameter $P \in \mathbb{R}$, $0 \leq p \leq 1$. Here we assign p a hyperprior that is uniform in the range of $[0.9, 0.99]$, to ensure that $\nu_i^{(k)}(\tau_i^{(k)})$ decreases rapidly with $\tau_i^{(k)}$. To connect $\nu_i^{(k)}(\tau_i^{(k)})$ with the prior on the material density, we invoke Bayesian regularisation.

4.2. *Bayesian regularisation.* The constraints on $\rho(\mathbf{x})$ can render the density to be embedded in a compact manifold $\mathcal{M} \in \mathbb{R}^3$, where the system variable $\Lambda \in \mathbb{R}^3$ defines \mathcal{M} as the surface on which (in general) a non-linear constraint $f(\Lambda) = 0$ holds true, $f: \mathbb{R} \rightarrow \mathbb{R}$, (Tibshirani 1996).

Chakrabarty (2010), discuss an application in which triaxially shaped, iso-density surfaces are invoked to reflect the model assumption that material in the system was stratified on triaxial ellipsoids. A non-negative system parameter (triaxial radius) $\lambda(\mathbf{x})$, ($\mathbf{x} \in \mathbb{R}^n$, $n \in \mathbb{Z}_+$, $\Lambda \in \mathbb{R}$), is defined and the prior used on the non-negative density $\rho(\mathbf{x})$, $\rho: \mathbb{R}^n \rightarrow \mathbb{R}$ is $\pi_0(\rho) \propto \exp\left(-\frac{1}{2}\langle \rho, \mathbf{S}^{-1} \rho \rangle\right)$, where the $n \times n$ covariance matrix \mathbf{S} is defined in terms of the diagonalised Hessian matrix \mathbf{H} such that $\mathbf{S}^{-1} = \mathbf{H}\mathbf{H}^T$ with $H_{ij} = 0$, $i \neq j$, $i, j = 1, \dots, n$ and $H_{ij} = \Delta_\lambda$ if $i = j$. Here Δ_λ is the Laplacian-Beltrami operator with respect to the variable Λ , i.e. $\Delta_\lambda := \frac{\partial^2}{\partial \Lambda^2}$. Thus, \mathbf{S}^{-1} is a symmetric, positive definite matrix so that it is the precision matrix. Thus, the Bayesian regularisation used in Chakrabarty (2010) is similar to the Bayesian regularisation discussed by Park & Casella (2008), Hans (2009) and Liu et. al (2011) (unpublished).

We invoke a similar prior structure in this work, when partial information about the topology of $\rho(\mathbf{x})$ is identified (see Equation 4.3 in Section 4 of the main text) by judging the geometric details of the $\langle \mathcal{P}(\cdot) \rangle$ operator.

We set the $N_{eng} \times N_{eng}$ precision matrix for any $i = 1, \dots, N_{data}$ to be

$$(4.4) \quad \begin{aligned} \mathbf{S}_i^{-1} &= \mathbf{H}_i \mathbf{H}_i^T \\ H_{i k \ell} &= \nu_i^{(k)} \cdot \nu_i^{(\ell)} \text{ if } k = \ell \\ H_{i k \ell} &= 0 \text{ if } k \neq \ell. \end{aligned}$$

Here $k, \ell = 1, \dots, N_{eng}$ and $H_{i k \ell}$ is the $k\ell$ -th element of \mathbf{H}_i . $\nu_i^{(k)}$ is defined in Equation 4.3.

The estimation of the unknown functions is performed by projecting the convolution of the functions in the forward problem, at each iteration, into the image space, at each ϵ_k , $k = 1, \dots, N_{eng}$. The likelihood is defined as a function of the distance between this projection at any k and the image $\{\tilde{I}_i^{(k)}\}_{i=1}^{N_{data}}$, for any $k = 1, \dots, N_{eng}$, along with the selected priors, in order to then define the posterior that is sampled from using Metropolis-Hastings. The unknowns are drawn from respective proposal densities in each iteration. Upon convergence, we present the estimates $\hat{\Xi}_i^{(k)}$ and $\hat{\eta}^{(k)}$ with 95%-highest probability density credible regions, ($\forall i = 1, \dots, N_{data}$, $k = 1, \dots, N_{eng}$).

4.3. *Correction function.* Since we want to learn the 3-D density structure of the material sample and the correction function simultaneously, it helps the identifiability of the solutions if $\eta(\mathbf{x})$ is assumed to be a global.

Thus, we define the correction function as independent of E and beam-pointing locations, and only depends upon the depth Z , i.e. it is $\eta(z)$, for a given material.

In the microscopy literature, the 2-D radiation density generated due to the material along an angle χ (to the vertical) is given by $Q \int_0^\infty \Psi(\rho z) \exp[-f(\chi)\rho z] d(\rho z)$, where $Q \in \mathbb{R}$, $Q > 0$ is a constant, $f(\chi) \propto 1/\sin(\chi)$ with an proportionality constant that is not known apriori and needs to be estimated using system-specific Monte Carlo simulations or approximations based on curve-fitting techniques; see Goldstein et al. (2003). $\Psi(\rho z)$ is the distribution of the variable (representing the ‘‘mass depth’’) ρz and is again not known apriori but can be estimated apriori, using Monte Carlo simulations of the system or from atomistic models. However, these simulations or model-based calculations are material specific and their viability in inhomogeneous material samples is questionable.

Our construct differs from this formulation in that we construct an infinitesimally small volume of depth δZ inside the material, at the point (X, Y, Z) . In the limit of $\delta z \rightarrow 0$, the density of the material inside this infinitesimally small volume is a constant, namely $\rho(X, Y, Z)$. Thus, the measured radiation density generated from this infinitesimally small volume in is $\rho(X, Y, Z)\eta(Z)\delta Z$. Thus, over this infinitesimal volume, our formulation ties in with the representation in microscopic theory, if we set $\eta(z)$ and $\Psi(\rho z) \exp[-f(\chi)\rho z]$ proportional; the difference lies in us defining the blurring function to depend only on Z - a simplifying model assumption for us.

Given the lack of modularity in the modelling of the relevant system parameters within the conventional approach, and the existence in the microscopy literature of multiple models that compare with each other in the relative improvement of the approximations involved (Goldstein et al. 2003; Merlet. 1994), it is meaningful to seek an estimate of the blurring function. As we will show in Section 4.8, assuming knowledge of $\eta(z)$ renders the problem well-posed but our ambition of trying to estimate the blurring function as well as the material density, will render the problem under-determined in the general case, within the paradigm of the data structure discussed above.

We set our correction function to be proportional to $\Psi(\rho z) \exp(-cz)$, where the material-dependent constant $C \in \mathbb{R}$ depends upon whether the considered image is in BSE (in which case C represents the BSE coefficient, often estimated with Monte-Carlo simulations) or X-rays (in which case it is the linear attenuation coefficients, tabulated for example at <http://physics.nist.gov/PhysRefData/XrayMassCoef/tab3.html>). A more detailed discussion is included in Appendix A. C is assigned a uniform hyperprior over the range $[10^{-4}, 10^{-2}] \mu\text{m}$ for BSE images (Wong & Elliott 1997; Goldstein et al. 2003) and $[0.01, 0.1] \mu\text{m}$ for X-ray images - these are the expected range for C , given the beam energies (~ 10 kV) and that we work with. Also, the shape of $\Psi(\rho z)$, as available in the literature, is emulated as a folded normal (Leone, Nottingham & Nelson 1961) and the corresponding prior on $\eta(z)$ is implemented in the non-parametric model of the correction function (see Appendix A). In the semi-parametric implementation, this available shape of $\Psi(\cdot)$ is acknowledged and $\eta(z)$ expressed as proportional to the product of an exponential and folded normal, given the relevant parameters; as discussed in details in Appendix B, there are effectively two such parameters, including the constant of proportionality and the mean of the folded normal, given that knowledge of $\Psi(0)$ is available in the microscopy literature and that in the relevant energies, $\exp(-cz) \approx 1$. Gaussian priors are placed on these two parameters.

It is to be noted that the available knowledge of $\Psi(0)$ - and thereby of $\eta(0)$ - allows for the identifiability of the amplitudes of $\rho(\mathbf{x})$ and $\eta(z)$. The details are discussed in Appendix A and Appendix B.

4.4. *Inversion details.* For any $i = 1, \dots, N_{data}$ and $k = 1, \dots, N_{eng}$, the surface of the ik -th interaction-volume is described by the equation $a_i^{(k)}(R, \theta, z) = 0$ where $R = \sqrt{(x - x_i^{(k)})^2 + (y - y_i^{(k)})^2}$, $\tan \theta = (y - y_i^{(k)}) / (x - x_i^{(k)})$. The ik -th voxel is defined to be the one whose intersection with the $Z=0$ plane is the square centred at $(x_i, y_i, 0)$, edges of length δ and depth $h^{(k)}$. By design, density inside the ik -th voxel is a constant, given the measured 2-D radiation density map, $\forall i = 1, \dots, N_{data}$, $k = 1, \dots, N_{eng}$. This construct equivalently, motivates the assumption that $\eta(z)$ is a constant within any voxel.

DEFINITION 4.1. For $z \in [h^{(k-1)}, h^{(k)})$, $\rho(x_i, y_i, z_i^{(k)}) = \xi_i^{(k)}$, $\forall i = 1, \dots, N_{eng}$, $k = 1, \dots, N_{eng}$, $h^{(0)} = 0$, where $\Xi|i, k$ is abbreviated as $\Xi_i^{(k)}$, $(\Xi_i^{(k)} \in \mathbb{R}, \Xi_i^{(k)}$ is a non-negative scalar for any i and k).

DEFINITION 4.2. For $z \in [h^{(k-1)}, h^{(k)})$ $\eta(z) = \eta^{(k)}$ $k = 1, \dots, N_{eng}$, where $h^{(0)} := 0$. Then, the functional of $\eta(z)$ that is relevant to the inversion of the image into the density is

$$(4.5) \quad \Phi^{(k)} := \int_0^{h^{(k)}} \eta(z) dz, \quad \forall k = 1, \dots, N_{eng}, \quad i = 1, \dots, N_{data}$$

$$\Phi^{(k)} = \sum_{j=1}^{j=k} \eta^{(j)} (h^{(j)} - h^{(j-1)}) \quad h^{(0)} := 0$$

In the context of the application to microscopy, atomic theory studies undertaken by Kanaya & Okamaya (1972) - suggest that the resting length $h^{(k)}$ (measured in μm), of a beam electron of energy E ($E = \epsilon_k$ measured in kV), inside material of mass density of D ($D = d$ measured in gm cm^{-3}), atomic number \mathcal{Z} and atomic weight A per gm per mole, is

$$(4.6) \quad h^{(k)} = \frac{0.0276 A \epsilon^{1.67}}{d \mathcal{Z}^{0.89}} \quad k \in \mathbb{Z}_+.$$

Here \mathcal{Z} is an integer valued constant, $\mathcal{Z} > 0$ while A and d are positive-definite real valued constants. As E increases, the depth and radial extent of the interaction-volume increases.

We introduce two classes of systems; for fixed values of all parameters but \mathcal{Z} ,

$$(4.7) \quad \begin{array}{ll} \text{if } \delta \geq R0^{(N_{eng})}|\mathcal{Z}, & \text{“high-Z” material} \\ \text{if } \delta < R0^{(N_{eng})}|\mathcal{Z}, & \text{“low-Z” material.} \end{array}$$

In our application we use Kanayama’s estimate for the electron penetration depth. Along with this, we make the assumption that the interaction-volume shape is hemi-spherical, i.e. if (x, y, z) lies on the the surface of the ik -th interaction-volume, then $(x - x_i^{(k)})^2 + (y - y_i^{(k)})^2 + z^2 = (h_i^{(k)})^2$. Microscopy literature suggests that even for low-Z materials, $R0^{(k)} \leq h^{(k)}$ so that we set $R0^{(k)} = h^{(k)} \forall k = 1, \dots, N_{eng}$ through this model assumption.

We develop three distinct models for the inversion of a given image. These models pertain to three cases that are distinguished by the spatial resolutions inherent to the imaging technique at hand, allowing for the learning of the density substructure over different length scales. Here $\hat{\Xi}_i^{(k)}$ is an abbreviation for the density estimate $\hat{\rho}(x_i, y_i, z_i^{(k)})$ in the ik -th voxel, and $\hat{\eta}^{(k)}$ for $\hat{\eta}(z_i^{(k)})$, to be used hereafter.

In the first case, $R0^{(k)} < \delta$, for $k = 1, \dots, N_{eng}$.

Resolution for the next model implies that for $k \leq k_{min}$, $R0^{(k)} < \delta$, but for $k = k_{in} + 1, \dots, N_{eng}$, $R0^{(k)} > \delta$. Then for $k = k_{min} + 1, \dots, N_{eng}$, we first approximate $\hat{\Xi}_i^{(k)}$ as the nearest neighbour average, i.e. the average over the azimuthal angle. This allows for effective dimensionality reduction of the model density during the spatial averaging over the extent of the ‘‘interaction volume’’.

The most difficult of the three cases is the one in which the imaging technique has a resolution that is so fine that multiple voxels fit inside the ik -th ‘‘interaction volume’’, $k = 1, \dots, N_{eng}$, $i = 1, \dots, N_{data}$.

4.5. 1st and 2nd models - Low resolution. Let us first consider the examples in which $\delta \sim R0^{(N_{eng})}$. The class of examples with $R0^{(N_{eng})} \sim 1\mu m$, pertain to the case when the system is imaged by an SEM in X-rays. The modelling in these techniques is typified by the ik -th interaction-volume sitting wholly or partly inside the ik -th voxel, $i = 1, \dots, N_{data}$, $k = 1, \dots, N_{eng}$.

For the high- Z case, the spatial resolution δ of the imaging technique is so coarse that voxel size (of length and width δ each) along the X and Y -axes, exceed the extent of the interaction-volume of the material for $E = \epsilon_{N_{eng}}$, i.e., $\delta \geq R0^{(k)}$, $\forall k = 1, \dots, N_{eng}$. Then the density inside the ik -th interaction-volume is $\Xi_i^{(k)}$, a constant, equal to the density inside the ik -th voxel, $i = 1, \dots, N_{data}$; $k = 1, \dots, N_{eng}$. Thus, dimensionality reduction is easily achieved in this case. Within the ik -th ‘‘interaction volume’’, density has no dependence on X and Y , but does vary with Z . Then Equation 2.1, with the integral over Z discretised, suggests the following.

$$I_i^{(k)} = \frac{1}{(R0^{(k)})^2} \int_0^{R0^{(k)}} dR R. \quad (4.8) \quad \left[\sum_{t=0}^{n(R)} \Xi_i^{(t)} \phi^{(t)} + \Xi_i^{(n(R)+1)} \phi^{(n(R)+1)} \frac{(R - R0^{(n(R)))}}{(R0^{(n(R)+1)} - R0^{(n(R)))})} \right].$$

where $n : \mathbb{R} \rightarrow \mathbb{Z}_+$ and $R0^{(n(R))} + \Delta(R) = \sqrt{(R0^{(k)})^2 - R^2}$, with $0 \leq \Delta(R) < R0^{(n(R)+1)} - R0^{(n(R))}$. Here $\Phi^{(t)} := \int_{h^{(t-1)}}^{h^{(t)}} \hat{\eta}(z) dz$ and $h^{(0)} := 0$. Also, the 2-D radiation density generated as a result of interactions within the ik -th interaction-volume is $I(x_i^{(k)}, y_i^{(k)})$, abbreviated as $I_i^{(k)}$, for $i = 1, \dots, N_{data}$, $k = 1, \dots, N_{eng}$.

However, for a low- Z materials, for any $i \in 1, \dots, N_{data}$, and $k > k_{in}$, the interaction-volume will spill out of the ik -th voxel into the neighbouring voxels. As a result, there will be contributions to the intensity $I_i^{(k)}$ from voxels that neighbour the ik -th voxel. In general, at a given Z , any bulk voxel has 8 such neighbouring voxels and when the ik -th voxel lies at the corner or edge of the material sample, the contribution to $I_i^{(k)}$ from itself and its nearest neighbours is different from when it is not; in either case, this contribution is easily computable by tracking

the geometry of the system. In general, there will be contribution from 9 voxels towards $I_i^{(k)}$ - these include the contribution from the ik -th voxel and its 8 nearest neighbours.

At any azimuth $\theta \in [0, 2\pi]$ and $R \in [R0^{(k-1)}, R0^{(k)})$, for $k > k_{in}$, $\bar{\Xi}^{(ik)}$ is approximated as θ -independent and defined as the weighted mean of $\{\bar{\Xi}_{m|i}^{(k)}\}_{m=1}^9$ - the densities of the neighbouring voxels of the ik -th voxel, where these neighbours are fully or partially enclosed within the hemispherical interaction-volume centred at $(x_i, y_i, 0)$ and of radius $R0^{(k)}$. The weight $w_{m|i}^{(k)}$ represents the fractional volume occupied by the m -th neighbouring voxel within this hemisphere, $m = 1, \dots, 9$, $k = 1, \dots, N_{eng}$, $i = 1, \dots, N_{data}$. Thus, for beam pointings on a corner or edge voxels there will be some m for which $w_{m|i}^k = 0$; also $w_{m|i}^{(k)} = 0 \forall m > 1$ for $k \leq k_{in}$, where the voxel containing the point (x_i, y_i, z) , $z \in [0, h_i^{(N_{eng})})$, is indexed by $m = 1$. The effect of this averaging over the nearest neighbours is equivalent to averaging over the azimuthal angle θ and results in the nearest-neighbour averaged or azimuthally averaged density $\bar{\Xi}^{(ik)}$ where

$$(4.9) \quad \bar{\Xi}^{(ik)} = \sum_{m=1}^9 \bar{\Xi}_{m|i}^{(k)} w_{m|i}^{(k)} \quad \text{for low-}\mathcal{Z} \text{ materials.}$$

Here, for any $k = 1, \dots, N_{eng}$, $w_{m|i}^{(k)}$ is the weight due to the m -th nearest neighbour of the ik -th voxel, and $\bar{\Xi}_{m|i}^{(k)}$ is the density of this ik -th voxel, $i = 1, \dots, N_{data}$. Thus, $m|i \in \mathbb{Z}_+$, for $m = 1, \dots, 9$ for any $i = 1, \dots, N_{data}$.

Then $I_i^{(k)} := \langle \mathcal{P}(\hat{\rho} * \hat{\eta}) \rangle_i^{(k)}$, $i = 1, \dots, N_{data}$, $k = 1, \dots, N_{eng}$ and

$$(4.10) \quad I_i^{(k)} = \frac{\int_0^{R0^{(k)}} \left[\int_0^{\sqrt{(R0^{(k)})^2 - R^2}} \bar{\Xi}^{(q(R)j(z))} \hat{\eta}(z) dz \right] R dR}{\int_0^{R0^{(k)}} R dR},$$

where $j : \mathbb{R} \rightarrow \mathbb{Z}_+$, $j(z) = 1, \dots, N_{eng}$ is a running variable representing the beam energy index as Z varies discretely over the range $[0, \sqrt{(R0^{(k)})^2 - R^2}]$, such that $h^{(j(z)-1)} \leq z < h^{(j(z))}$. Also, $q : \mathbb{R} \rightarrow \mathbb{Z}_+$, $q(R) = 1, \dots, N_{data}$ is a running variable representing the beam energy index as R varies discretely over the range $[0, R0^{(k)}]$, such that $R0^{(q(R)-1)} \leq R < R0^{(q(R))}$.

For low- \mathcal{Z} materials, Equation 4.8 is valid for $k \leq k_{in}$, where $R0^{(k_{in})} \leq \delta < R0^{(k_{in}+1)}$. For $k > k_{in}$ we can no longer assume uniform density within the full radial extent of the "interaction volume" and in this case,

$$(4.11) \quad \tilde{I}_i^{(k)} = \frac{1}{(R0^{(k)})^2} \sum_{n=1}^k [(R0^{(n)})^2 - (R0^{(n-1)})^2] f_n \quad \text{if } k > k_{in}$$

$$\text{where } f_n := \left[\sum_{t=0}^{j_n^{(k)}} \bar{\Xi}^{(nt)} \phi^{(t)} + \bar{\Xi}^{(n j_n^{(k)} + 1)} \phi^{(j_n^{(k)} + 1)} \frac{\Delta_n}{(R0^{(j_n^{(k)} + 1)} - R0^{(j_n^{(k)})})} \right]$$

$$\text{with } j_n^{(k)} \in \mathbb{Z}_+ : \sqrt{[R0^{(k)}]^2 - [R0^{(n)}]^2} = R0^{(j_n^{(k)})} + \Delta_n$$

$$\text{and } 0 \leq \Delta_n < R0^{(j_n^{(k)} + 1)} - R0^{(j_n^{(k)})}.$$

$\forall k = 1, \dots, N_{eng}, \forall i = 1, \dots, N_{data}$.

The additional difficulty about the low- \mathcal{Z} case arises from the fact that once $\{\bar{\Xi}^{(ik)}\}_{k=1}^{N_{eng}}$ are estimated using Equation 4.11, for any $i = 1, \dots, N_{data}$, $\{\Xi_i^{(k)}\}_{k=1}^{N_{eng}}$ needs to be learnt. This is achieved numerically, using Equation 4.9. In this equation for any $i = 1, \dots, N_{data}$, $\bar{\Xi}^{(ik)}$ is known (learnt using Equation 4.11) as a linear combination of the known and $w_{m|i}^{(k)}$ and unknown $\Xi_{m|i}^{(k)}$, for any $k = 1, \dots, N_{eng}$ and $m = 1, \dots, 9$. For any $k = 1, \dots, N_{eng}$ Equation 4.9 is re-phrased as:

$$(4.12) \quad \bar{\Xi}^{(k)} = \mathbf{W}^{(k)} \Xi^{(k)}$$

where $\bar{\Xi}^{(k)}$ is an N_{data} -dimensional vector $(\bar{\Xi}^{(1k)}, \bar{\Xi}^{(2k)}, \dots, \bar{\Xi}^{(N_{data}k)})^T$ and $\Xi^{(k)}$ is the N_{data} -dimensional vector $(\Xi^{(1k)}, \Xi^{(2k)}, \dots, \Xi^{(N_{data}k)})^T$. $\mathbf{W}^{(k)}$ is an $N_{data} \times N_{data}$ matrix, any row of which has a maximum of 9 non-zero values (given the maximum of 9 nearest neighbours of the ik -th voxel, $i = 1, \dots, N_{data}$, $k = 1, \dots, N_{eng}$). Thus,

$$(4.13) \quad \begin{aligned} \mathbf{W}_{ij}^{(k)} &= 0 & \text{if } j \notin \{1|i, 2|i, \dots, 9|i\} \\ \mathbf{W}_{ij}^{(k)} &= w_{j|i}^{(k)} & \text{if } j \in \{1|i, 2|i, \dots, 9|i\}. \end{aligned}$$

Thus, Equation 4.12 can be solved by inverting the $\mathbf{W}^{(k)}$ matrix, $\forall k = 1, \dots, N_{eng}$, so that

$$(4.14) \quad \Xi^{(k)} = (\mathbf{W}^{(k)})^{-1} \bar{\Xi}^{(k)}$$

REMARK 4.1. *The nearest neighbour structure of the ik -th voxel and the jk -th voxel are independent, for any $i \neq j$, $i, j = 1, \dots, N_{data}$*

$\implies W_i^{(k)}$ and $W_j^{(k)}$ are linearly independent $\forall i \neq j$

where $W_l^{(k)}$ is an N_{data} -d vector, the t -th component of the $W_l^{(k)}$ is

$$(4.15) \quad \begin{aligned} w_{lt}^{(k)} &= 0 & \text{if } t \notin \{1|l, 2|l, \dots, 9|l\} \\ w_{lt}^{(k)} &= w_{t|l}^{(k)} & \text{if } t \in \{1|l, 2|l, \dots, 9|l\}, \end{aligned}$$

for any $l = 1, \dots, N_{data}$. This implies that row rank of $(\mathbf{W}^{(k)})$ is full, i.e. $(\mathbf{W}^{(k)})^{-1}$ exists.

Although the deterministic solution of $\Xi_i^{(k)}$ from $\bar{\Xi}^{(ik)}$ is suggested in Equation 4.14, the inversion of the $N_{data} \times N_{data}$ matrix is prohibitively cost-intensive. Given this, we resort to the learning of $\Xi_i^{(k)}$, $k = 1, \dots, N_{eng}$, $i = 1, \dots, N_{data}$, directly in the forward problem, by using a trial $\rho(\mathbf{x})$ to define $\bar{\Xi}^{(ik)}$ (from Equation 4.9 and the known weights from the nearest neighbours for any $i = 1, \dots, N_{data}$), which is then used to define the spatially averaged projection of $\rho(\mathbf{x}) * \eta(z)$, the mismatch of which with the data defines the likelihood (see Section 4.7).

4.6. *3rd model - Fine resolution.* In certain imaging techniques, such that imaging in BSE by an SEM or FESEM, the resolution $\delta \ll R0_i^{(N_{eng})}$, $\forall i = 1, \dots, N_{data}$. In such cases, the modelling used in cases of coarser resolution, for the averaging

over the interaction-volume, cannot be used. Knowing the shape of the interaction-volume, it is possible to identify the voxels that live partly or wholly inside the ik -th interaction-volume as well as compute the fractional volume of each such voxel inside the ik -th interaction volume.

For this model, the projection equation is written in terms of the coordinates of a point (x, y, z) inside the ik -th interaction volume that is centred at $(x_i, y_i, 0)$, so that,

(4.16)

$$\tilde{I}_i^{(k)} = \frac{1}{(R0^{(k)})^2} \int_{x=0}^{R0^{(k)}} dx \int_{y=0}^{\sqrt{(R0^{(k)})^2 - x^2}} dy f(x, y), \quad f : \mathbb{R} \times \mathbb{R} \longrightarrow \mathbb{R}$$

$$f(x, y) = \sum_{t=0}^{j(x,y)} \Xi_{n(x,y)}^{(t)} \phi^{(t)} + \Xi_{n(x,y)}^{(j(x,y)+1)} \phi^{(j(x,y)+1)} \frac{\Delta(x, y)}{(R0^{(j(x,y)+1)} - R0^{(j(x,y))})}$$

where $j : \mathbb{R} \times \mathbb{R} \longrightarrow \mathbb{Z}_+ : \sqrt{[R0^{(k)}]^2 - x^2 - y^2} = R0^{(j(x,y))} + \Delta(x, y)$ with $0 \leq \Delta(x, y) < R0^{(j(x,y)+1)} - R0^{(j(x,y))}$ and $n : \mathbb{R} \times \mathbb{R} \longrightarrow \mathbb{Z}_+$ such that

$$n(x, y) = (\text{int}) \left(\frac{y_i}{\delta} + 1 \right) \sqrt{N_{data}} + (\text{int}) \left(\frac{x_i}{\delta} + 1 \right) \sqrt{N_{data}} + n_x + n_y,$$

where $n_x, n_y \in \mathbb{Z}_+$,

$$n_x = \min \left[\sqrt{N_{data}}, (\text{int}) \left(\frac{x}{\delta} + 1 \right) \right] \text{ if } x > 0,$$

$$n_x = \max \left[1, (\text{int}) \left(\frac{x}{\delta} + 1 \right) \right] \text{ if } x < 0,$$

$$n_y = \min \left[\sqrt{N_{data}}, (\text{int}) \left(\frac{y}{\delta} + 1 \right) \sqrt{N_{data}} \right] \text{ if } y > 0$$

$$n_y = \max \left[1, (\text{int}) \left(\frac{y}{\delta} + 1 \right) \sqrt{N_{data}} \right] \text{ if } y < 0.$$

The above equations are true $\forall k = 1, \dots, N_{eng}, \forall i = 1, \dots, N_{data}$.

4.7. Inference. In this work, we learn the unknown functions by implementing $\langle \mathcal{P}(\rho * \eta) \rangle$ in the forward problem; in particular, the learning is performed using the mismatch between the data $\{\tilde{I}_i^{(k)}\}_{k=1; i=1}^{N_{eng}; N_{data}}$ and $\langle \mathcal{P}(\rho * \eta) \rangle$, in terms of which, the likelihood of the data, given the model, is defined. In the forward problem, the current material density and blurring function are convolved, and the projection of this convolution spatially averaged, for the three respective models, as modelled in Equation 4.8, Equation 4.11 and Equation 4.16, to compute $I_i^{(k)}$, for any $i = 1, \dots, N_{data}, k = 1, \dots, N_{eng}$. Thus, the mismatch that the likelihood is defined in terms of, is that between the data $\tilde{I}_i^{(k)}$ and $I_i^{(k)}$.

We choose to work with a Gaussian likelihood:

(4.17)

$$\mathcal{L}(I_i^{(k)} | \rho(x_i, y_i, z_i^{(k)}), \Phi(z^{(k)})) = \frac{1}{\sqrt{2\pi}\sigma_i^{(k)}} \exp \left[-\frac{(I_i^{(k)} - \tilde{I}_i^{(k)})^2}{2(\sigma_i^{(k)})^2} \right],$$

$$k = 1, \dots, N_{eng}, i = 1, \dots, N_{data}$$

where $I_i^{(k)}$ is given by the right hand sides of the first equations in the set of equations (Equation 4.8, Equation 4.11 and Equation 4.16). Here $\sigma_i^{(k)}$ is maintained a constant $\forall i = 1, \dots, N_{data}, k = 1, \dots, N_{eng}$. Also, $\sigma_i^{(k)}$ is varied from 10 to 1 times the measurement error in $\tilde{I}_i^{(k)}$.

Towards the learning of the unknown functions, the density of the posterior measure, given the image data, is defined using Bayes rule, while assuming that the spatial average of the projection of the convolution of the unknowns, over the ik -th “interaction volume”, are conditionally *iid* so that

$$(4.18) \quad \pi(\Xi_1^{(1)}, \dots, \Xi_1^{(N_{eng})}, \dots, \Xi_{N_{data}}^{(1)}, \dots, \Xi_{N_{data}}^{(N_{eng})}, \Phi^{(1)}, \dots, \Phi^{(N_{eng})} | \tilde{I}_1^{(1)}, \dots, \tilde{I}_{N_{data}}^{(N_{eng})}) \propto \prod_{i=1}^{N_{data}} \prod_{k=1}^{N_{eng}} \mathcal{L}(\tilde{I}_i^{(k)} | \rho(x_i, y_i, z_i^{(k)}), \Phi(z^{(k)})) \pi_0(\Xi_1^{(1)}, \dots, \Xi_{N_{data}}^{(N_{eng})}) \nu_0(\Phi^{(1)}, \dots, \Phi^{(N_{eng})})$$

where $\pi_0(\Xi_1^{(1)}, \dots, \Xi_{N_{data}}^{(N_{eng})})$ is the joint prior probability density of $\rho(\mathbf{x})$ in our models. As discussed in Section 4.1, the prior on the density reflects the geometrical details of the models. Also, $\nu_0(\Phi^{(1)}, \dots, \Phi^{(N_{eng})})$ is the prior of the discretised function $\Phi(z)$, defined in Equation 4.5. This prior structure is discussed in Section 4.3.

Once the posterior probability of the material density structure and blurring function is defined, we then use the adaptive Metropolis-Hastings algorithm of Haario, Laine, Mira & Saksman (2006) to generate posterior samples.

At the n -th iteration, $n = 1, \dots, N_{max}$, $\Xi_i^{(k)}$ is proposed from a folded normal density². The proposed density in the n -th iteration, in the ik -th voxel is

$$(4.19) \quad \tilde{\Xi}_i^{(k)} | n \sim \mathcal{N}_F(\mu_i^{(k)} | n, \varsigma_i^{(k)} | n) \quad k = 1, \dots, N_{eng}$$

while the current density in this voxel at the n -th iteration is defined as $\Xi_i^{(k)} | n$. We choose the parameters of this proposal density to be

$$(4.20) \quad \begin{aligned} \mu_i^{(k)} | n &= \Xi_i^{(k)} |_{n-1}, \quad \forall k = 1 \dots, N_{eng}, i = 1, \dots, N_{data}, n = 1, \dots, N_{max} \\ (\varsigma_i^{(k)} | n)^2 &= \frac{\sum_{p=n_0}^{n-1} (\Xi_i^{(k)} | p)^2}{n - n_0} - \left[\frac{\sum_{p=n_0}^{n-1} (\Xi_i^{(k)} | p)}{n - n_0} \right]^2 \quad \text{if } n \geq n_0 \\ &= T \Xi_i^{(k)} |_0 \quad \text{if } n < n_0 \end{aligned}$$

The random variable T is considered to be uniformly distributed, i.e. $T \sim U(0, 1]$. We choose $\Xi_i^{(k)} |_0$ by assigning constant density to the voxels that constitute the ik -th interaction-volume, $k = 1 \dots, N_{eng}$, $i = 1, \dots, N_{data}$. Thus, for $n \geq n_0$, the proposal density is adaptive, (Haario et al. 2006). We choose $n_0 = 10^4$ and N_{max} is of the order of 8×10^5 .

When a non-parametric model for the correction function is used, C and η_0 are proposed from exponential proposal densities with rate parameters $(s_1 | n)$ and $(s_2 | n)$ respectively, $S_1, S_2 \in \mathbb{R}$, $S_1, S_2 \geq 0$ (see Appendix A). When a semi-parametric model for the correction function is used, $\eta(z)$ is calculated as given in Equation of Appendix B, conditional on the values of 2 parameters that are proposed at each iteration - \tilde{Q}_n and $\tilde{\eta}_0 | n$ in the n -th iteration; \tilde{Q}_n and $\tilde{\eta}_0 | n$ are

²The distribution $\mathcal{N}_F(a, b)$ is the folded normal distribution with mean $a \in \mathbb{R}$, $a > 0$ and standard deviation $b \in \mathbb{R}$, $b > 0$ (Leone et al. 1961)

each proposed from independent exponential proposal densities with constant rate parameters.

The state space of the fully discretised model is $N_{data} \times N_{eng} + N_{eng}$ -dimensional while for the semi-parametric implementation of the correction function, the state-space is $N_{data} \times N_{eng} + 2$ -dimensional, respectively. The inference is performed by sampling from the high dimensional posterior (Equation 4.18) using Metropolis-within-Gibbs block update, (Gilks & Roberts 1996; Chib & Greenberg 1995). Let the state at the n iteration be $\varepsilon_n = \{\Xi_i^{(1)}|_n, \dots, \Xi_{N_{data}}^{(N_{eng})}|_n, \Phi^{(1)}|_n, \dots, \Phi^{(N_{eng})}|_n\}$. For the implementation of the block Metropolis-Hastings, we partition the state vector ε_n into $(\varepsilon_n^{\Xi}, \varepsilon_n^{\Phi})$, where $n = 1, \dots, N_{burnin}, \dots, N_{max}$. (We typically use $N_{max} > 8 \times 10^5$ and $N_{burnin} = 1 \times 10^5$). Then, the state ε_{n+1} is given by the successive updating of the two blocks: $\varepsilon_{n+1} = (\varepsilon_{n+1}^{\Xi}, \varepsilon_{n+1}^{\Phi})$ where $\varepsilon_{n+1}^{\Xi} = \{\Xi_i^{(1)}|_{n+1}, \dots, \Xi_{N_{data}}^{(N_{eng})}|_{n+1}\}$ and $\varepsilon_{n+1}^{\Phi} = \{\Phi^{(1)}|_{n+1}, \dots, \Phi^{(N_{eng})}|_{n+1}\}$.

4.8. *Posterior measure in small noise limit.* Recalling the nature of the convolution of $\rho(\mathbf{x})$ and $\eta(z)$, and the subsequent spatial-averaging and projection from Equation 4.16, we write that for the constant resolution δ of the imaging technique under consideration,

$$(4.21) \quad I_i^{(k)} = \sum_{l=1}^{g(i,k)} \delta \sum_{p=1}^{n(i,k,l)} \delta \sum_{q=1}^{m(p,k)} a_q \Xi_{f(p,i)}^{(q)} \phi^{(q)}$$

where a general voxel inside the ik -th interaction-volume is marked as being p voxels away from the centre of the ik -th interaction-volume along the X -axis and ℓ voxels away from this centre along the Y -axis. Along the X -axis, the location index of the voxel furthest from this centre is a known function $g : \mathbb{Z}_+ \times \mathbb{Z}_+ \rightarrow \mathbb{Z}_+$. For a given X -axis location index ℓ , the maximal separation along the Y -axis is $n(i, k, \ell)$, $n : \mathbb{Z}_+ \times \mathbb{Z}_+ \times \mathbb{Z}_+ \rightarrow \mathbb{Z}_+$, $n(i, k, \ell) > 0$. The location index of this voxel on the $Z=0$ plane, is $f(p, \ell)$, where $f : \mathbb{Z}_+ \times \mathbb{Z}_+ \rightarrow \mathbb{Z}_+$ is a known integer-valued function. For a given beam energy ϵ_k , this voxel allows for a maximal depth that depends on its location on the $Z=0$ plane and k - we refer to this maximal depth as $m(f(p, \ell), k)$, which is given as $m : \mathbb{Z}_+ \times \mathbb{Z}_+ \rightarrow \mathbb{Z}_+$ $m(f, k) > 0$, $\sqrt{(R0^{(k-1)})^2 - f(p, \ell)^2} \leq m(f(p, \ell), k) < \sqrt{(R0^{(k)})^2 - f(p, \ell)^2}$. For a given voxel, in this ik -th interaction-volume, ($i = 1, \dots, N_{data}$, $\ell = 1, \dots, N_{eng}$)

$$(4.22) \quad \begin{aligned} a_q &= 1 & \text{for } q < m(s, k), \\ a_q &< 1 & \text{for } q = m(s, k), \\ a_q &= 0 & \text{for } q > m(s, k), \end{aligned} \quad \text{where} \\ s := f(p, \ell), \quad s \in \mathbb{Z}_+$$

With the aim of investigating the posterior probability density in the small noise limit, we recall the chosen priors for $\rho(\mathbf{x})$ (Section 4.1, 4.2) and $\Phi(z)$ (Section 4.3), and that the likelihood of the image data for all beam energies and beam locations is

$$(4.23) \quad \mathcal{L} = \prod_{i=1}^{N_{data}} \prod_{k=1}^{N_{eng}} \frac{1}{\sqrt{2\pi}\sigma_i^{(k)}} \exp \left[-\frac{(\tilde{I}_i^{(k)} - I_i^{(k)})^2}{2(\sigma_i^{(k)})^2} \right]$$

THEOREM 4.1. *In the limit of $\sigma_i^{(k)} \rightarrow 0$, the joint posterior probability density for the material density and blurring function, given the image data, for all beam locations ($i = 1, \dots, N_{data}$) and all ϵ_k $k = 1, \dots, N_{eng}$, reduces to a product of $N_{data} \times N_{eng}$ Dirac measures, with the ik -th measure centred at the solution to the equation $\tilde{I}_i^{(k)} = I_i^{(k)}$, $\forall i = 1, \dots, N_{data}$, $k = 1, \dots, N_{eng}$, where δ is the smallest length resolved by the imaging technique under consideration.*

PROOF. Logarithm of the posterior of the discretised nonparametric model is

$$(4.24) \quad \log \pi(\Xi_1^{(1)}, \dots, \Xi_{N_{data}}^{(N_{eng})}, \Phi^{(1)}, \dots, \Phi^{(m)} | \tilde{I}_1^{(1)}, \dots, \tilde{I}_{N_{data}}^{(N_{eng})}) \propto$$

$$(4.25) \quad \sum_{i=1}^{N_{data}} \sum_{k=1}^{N_{eng}} \left[-\log \sigma_i^{(k)} - \left(\frac{(\tilde{I}_i^{(k)} - I_i^{(k)})^2}{2(\sigma_i^{(k)})^2} \right) \right] - \sum_{k=1}^{N_{eng}} \left[\frac{(\phi^{(k)} + \eta 0^{(k)})^2}{2N(s^{(k)})^2} \right]$$

$$(4.25) \quad - \sum_{i=1}^{N_{data}} \sum_{k=1}^{N_{eng}} \left[\frac{\langle \Xi_i^{(k)}, S_i^{-1} \Xi_i^{(k)} \rangle}{2} \right] + A.$$

where $A \in \mathbb{R}$ is an arbitrary constant. Thus,

$$(4.26) \quad \lim_{\sigma_i^{(k)} \rightarrow 0} \pi(\Xi_1^{(1)}, \dots, \Xi_{N_{data}}^{(N_{eng})}, \Phi^{(1)}, \dots, \Phi^{(m)} | \tilde{I}_1^{(1)}, \dots, \tilde{I}_{N_{data}}^{(N_{eng})}) \propto$$

$$(4.26) \quad \lim_{\sigma_i^{(k)} \rightarrow 0} \prod_{i=1}^{N_{data}} \prod_{k=1}^{N_{eng}} \frac{1}{\sigma_i^{(k)}} \exp \left[-\frac{(\tilde{I}_i^{(k)} - I_i^{(k)})^2}{2(\sigma_i^{(k)})^2} \right]$$

The right hand side of this equation is the Dirac delta function centred at $\tilde{I}_i^{(k)} = I_i^{(k)}$, $\forall i = 1, \dots, N_{data}$, $k = 1, \dots, N_{eng}$. Thus, the posterior probability density reduces to a product of Dirac measures for each ik , with each measure centred on the solution of $\tilde{I}_i^{(k)} = I_i^{(k)}$. \square

REMARK 4.2. *The convergence of the posterior in the small noise limit, to the Dirac measure is due to our designing of the imaging experiment to generate multiple images at distinct beam energies, resulting in the the matching of dimensionality of the image and function spaces as well as due to the linearity of the spatial averaging+projection operator (see Equation 4.21) and the reduction of the convolution of the unknown functions to a product form, as is achieved in our discretised model.*

4.9. Quantification of deviation from uniqueness of learnt functions. From Theorem 4.1, we realise that the product of the estimated density $\hat{\Xi}$ and estimated functional of the correction function, $\hat{\Phi}$, is unique in the small noise limit. Assuming that measurement error of the data implemented in the estimation falls within the small noise limit, we realise that deviation from uniqueness in $\hat{\Xi}$ and $\hat{\Phi}$ are not independent. In fact, if the unique values of these functions, at any beam location index i and beam energy index k are $\xi_i^{(k)}$ and $\phi^{(k)}$, then Theorem 4.1 implies that $\hat{\xi}_i^{(k)} \times \hat{\phi}^{(k)}$ is unique. We view the values of the estimated function as lying in respective credible regions of width $\Delta(\hat{\xi}_i^{(k)})$ and $\Delta(\hat{\phi}^{(k)})$, with the unique solutions to these unknowns accommodated within such ranges. Then the maximal deviation

from uniqueness in the solutions would imply $[\Delta(\hat{\xi}_i^{(k)}) + \xi_i^{(k)}] \times [\Delta(\hat{\phi}^{(k)}) + \phi^{(k)}]$ is learnt uniquely (Theorem 4.1). This reduces to the result that maximal deviation from uniqueness of the estimate of the density is

$$(4.27) \quad \Delta(\hat{\xi}_i^{(k)}) \approx \frac{\Delta(\hat{\phi}^{(k)})\phi^{(k)}}{\xi_i^{(k)}}$$

$\forall i = 1, \dots, N_{data}, k = 1, \dots, N_{eng}$, where we have assumed that the maximal deviations from the unique solutions are small enough to ensure that the product $\Delta(\hat{\xi}_i^{(k)})\Delta(\hat{\phi}^{(k)})$ is small enough to be negligible, compared to $\Delta(\hat{\xi}_i^{(k)})\hat{\phi}^{(k)} + \Delta(\hat{\phi}^{(k)})\hat{\xi}_i^{(k)}$. Under this assumption, Equation 4.27 indicates that the non-uniqueness of estimate of the material density depends linearly on that of the blurring function which is directly determined by the strength of the priors placed on $\eta(z)$. Also, the equation suggests that voxels that harbour higher material densities are the voxels for which the solution for density is better constrained than voxels in which the material density is lower. It is to be noted that this last statement is made in reference to a comparison across voxels for a given material density structure, and does not say anything about the relative superiority of the method as far as applicability to a sparse material density structure over a dense one is concerned.

In particular, when the semi-parametric model of $\eta(z)$, is implemented, the underdeterminedness of the problem is low (compared to when the non-parametric model is used) - the ratio of number of data values to unknown model parameters is then $N_{eng} \times N_{data} / N_{eng} \times N_{data} + 2$. Thus, for typical values of 100 and 10 for N_{data} and N_{eng} respectively, this ratio is about 0.998 for the semiparametric model for $\eta(\cdot)$ and about 0.9823 for a nonparametric model for $\eta(\cdot)$. Considering this ratio as a parametrisation of the underdetermined-ness of the problem - as in Donoho & Tanner (2005) - we expect that the the 95% HPD credible regions that we advance for our estimates will include the deviation from uniqueness. Such an expectation is more likely to be true when the semiparametric, rather than the nonparametric model for the correction function is used.

We demonstrate the effect of these priors by working with the non-parametric model for the correction function in implementation of simulated data corresponding to the low resolution cases while we show the effect of both the non-parametric as well as the semi-parametric models of $\eta(\cdot)$, relevant to an application of the simulated high-resolution data (SEM image data).

5. Illustration on real SEM data. In this section we discuss the application of the advanced methodology towards the learning of the 3-D density and correction function by inverting 11 BSE images of a brick of Nickel (Ni) and Silver (Ag) nanoparticles, taken with an SEM (Leica, Stereoscan 430), at 11 distinct beam energies $\epsilon = 10, 11, \dots, 20\text{kV}$. The brick was prepared by the drop-cast method in the laboratory. The resolution of BSE imaging with the used SEM - and this resolution can be much worse than that for images with SE (Reed 2005) - is ≈ 50 nm. The 11 images are depicted in the attached supplementary information. We sample two distinct areas from the images, resulting in two different image data sets. The first data D_1 comprises an area of size $101\text{pixels} \times 101\text{pixels}$, with the pixels seated along specified rows and columns in each of the 11 images; we scale the pixels to physical locations of $-2.5 \mu\text{m}$ to $2.5 \mu\text{m}$ along the horizontal axis

(X -axis) as well as along the vertical axis (Y -axis), at intervals of $0.05 \mu\text{m}$ which is the resolution of the used imaging technique. The second data D_2 comprises a much smaller area - of size $21\text{pixels} \times 21\text{pixels}$, between a different (from that corresponding to D_1) set of rows and columns in the 11 images; the pixels are considered to range from $-1 \mu\text{m}$ to $1 \mu\text{m}$. Both D_1 and D_2 express the intensity $\tilde{I}_i^{(k)}$, which is a measure of the surface density of the back scattered electrons in the i -th pixel of the image taken with beam energy ϵ_k , where $k = 1, \dots, 11$ and $i = 1, \dots, 101^2$ for D_1 and $i = 1, \dots, 21^2$ for D_2 , $i = 1, \dots, 101^2$.

The learning of the material density of a nanostructure is very useful for device engineers engaged in employing such structures in the realisation of electronic devices; lack of consistency among measured electronic characteristics of the formed devices is tantamount to deviation from a standardised device behaviour and such can be predicted if heterogeneity in the depth distribution of nanoparticles is identified. Only upon the receipt of quantified information about the latter, is the device engineer able to motivate adequate steps. In addition, such information holds potential to shed light on the physics of interactions between nanoparticles.

If the calibration of this measure of the intensity is available, against physical units of surface density (of the BSE), then we could express the measured intensity map - as manifest in the recorded image - in relevant physical units. In that case, the learnt density could be immediately expressed in physical units. However, such a calibration is not available to us. In fact, in this method, the learnt density is scaled in the following way. The quantification of $\Psi(0)$ from microscopy theory (Merlet, 1994) suggests using the normalisation factor for $\Phi(z)$ is $\approx \hat{\Phi}^{(1)}/0.325$ where $\hat{\Phi}^{(1)}$ is the learnt function in the first Z -bin. The arithmetic mean of the atomistic parameters of Ni and Ag is used in this calculation. The (discretised) $\Phi(z)$ function, thus normalised, is then in the physical units of μm . The normalisation for the density is then the reciprocal of the above factor so that once normalised, the density is in units of μm^{-3} . The intensity of the BSE image is a measure of the number density, rather than the mass density in a bi-element material like the one we analyse here. Hence we learn the volume number density in each voxel.

The configuration that the constituent nanoparticles are expected to relax into, is due to several factors, including contribution from the surface effects - the surfaces of nanoparticles are active - this encourages interactions, resulting in a clustered configuration. Additionally, gravitational forces that the nanoparticle aggregates sediment under, are also active³, with the nanoparticle diameter responsible for determining the relative importance of the different physical influences (Joly-Puttez 2011). Thus, in general, along the Z coordinate, we expect a clustered configuration, embedded within layers. This is what we see in the representation of the learnt density in the $X - Z$ plane, when the image data D_1 and D_2 are inverted; see Figure 2. The spatially-averaged+projections of the same are and the correction functions learnt from the two data sets from the two non-overlapping parts of the images, are depicted in Figure 5. The concurring of the learnt correction functions is encouraging. The semi-parametric model for the correction function is implemented.

³Other relevant effects include viscosity and Brownian motion.

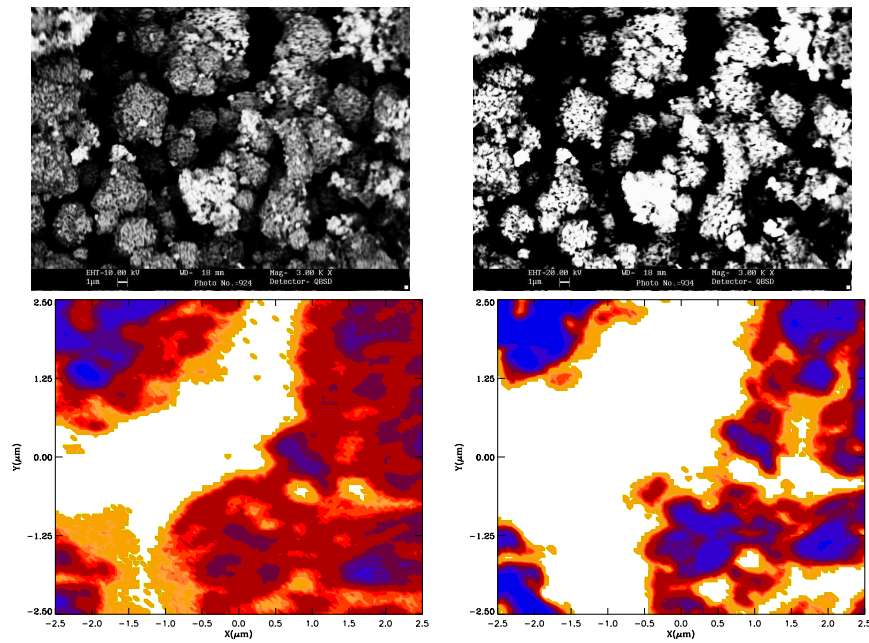


FIG 1. The top panels display two of the 11 BSE images of the prepared blend of Ni-Ag nanoparticles, taken with an SEM, at beam energies of 20 kV (right) and 10 kV (left). A $5 \mu\text{m} \times 5 \mu\text{m}$ area was identified in each of the 11 BSE images, to form the data D_1 . The distribution of the measured BSE intensity over this area, for beam energies of 10 kV and 20 kV are shown in the left and right panels of the lower row.

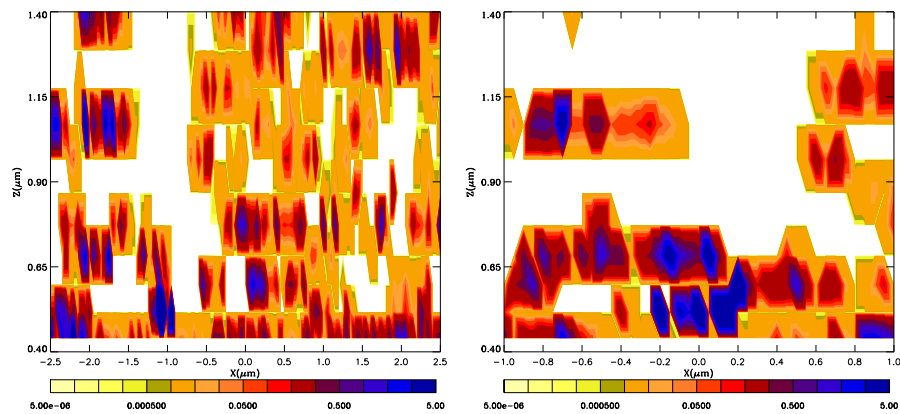


FIG 2. The left and right panels show the slice of the learnt three dimensional material density in the $X - Z$ plane, at the posterior mode, from inversion of image data D_1 and D_2 respectively. The data are obtained by imaging a brick of Nickel and Silver nanoparticles in BSE, at resolution of 50 nm, at 11 different beam energies 10 kV, . . . , 20 kV. D_1 and D_2 comprise 101×101 pixels and 41×41 pixels respectively. The labels on the colour-bar are number density values, in units of μm^{-3} .

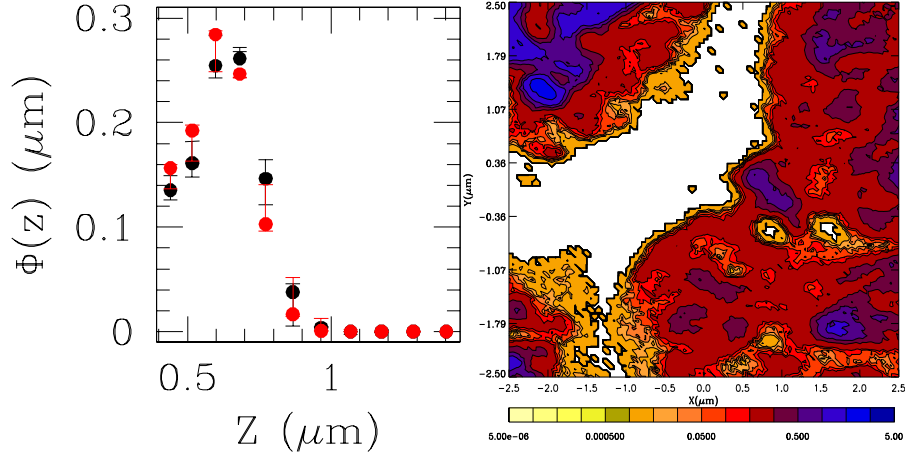


FIG 3. The right panel shows the spatially-average+projection of the material density learnt using image data D_1 in filled contours, (at the mode of the posterior) with the real image data D_1 overlaid in black solid contours. The left panel shows the correction functions learnt from data D_1 and D_2 in black and red respectively. The error bars in this plot represent the 95% highest probability density credible region of the estimate.

5.1. MCMC Diagnostics. In this section we include various diagnostics of an MCMC chain that was run until convergence, using the image data D_1 . These include trace of the likelihood (upper panel in Figure 4), an autocorrelation plot (lower panel of Figure 4) and histograms of multiple learnt parameters - $\Xi_{50}^{(1)}$, $\eta^{(1)}$ - from 1000 steps, in two distinct parts of the chain, namely, for step number $N \in [1599001, 1600000]$ and $N \in [799001, 800000]$, respectively (Figure 5). The histograms of the likelihood over these two separated parts of the chain are also presented in this figure.

6. Discussion. Solving an inverse problem $I = \mathcal{P}(\rho) + \varepsilon$ involves the inversion of the given data $I \in \mathcal{D} \subseteq \mathbb{R}^{n-1}$ (marked by noise $\varepsilon \in \mathbb{R}^{n-1}$), in order to construct the unknown density $\rho \in \mathcal{H} \subseteq \mathbb{R}^n$, the convolution of which with a known kernel results in the data in the first place. Cast as an integral equation, a deconvolution problem such as this, would be represented by Volterra or Fredholm integral equations of the first kind. In contrast to typical inverse problems, here we deal with the case of the image formed as a result of multiple integrals over the convolution of two unknown functions (Equation 2.1). This renders the problem at hand different, and essentially more difficult than typically reported versions of such inverse problems. The novelty of the methodology advanced above constitutes the attempted solution of this atypically hard problem, while ensuring uniqueness of the solution of the product of the unknowns as well as a quantification of the deviation from uniqueness in the estimates of each learnt function.

From the point of view of 3-D structure modelling, using images taken with bulk microscopic imaging techniques⁴, (such as Scanning Electron Microscopy, Electron Probe Microscopy), our aim here supercedes mere identification of the geometrical distribution of the material (the microstructure); we aim to estimate the material density structure. Conventionally, Monte Carlo simulation studies of microstructure are undertaken; convolution of such simulated microstructure, with

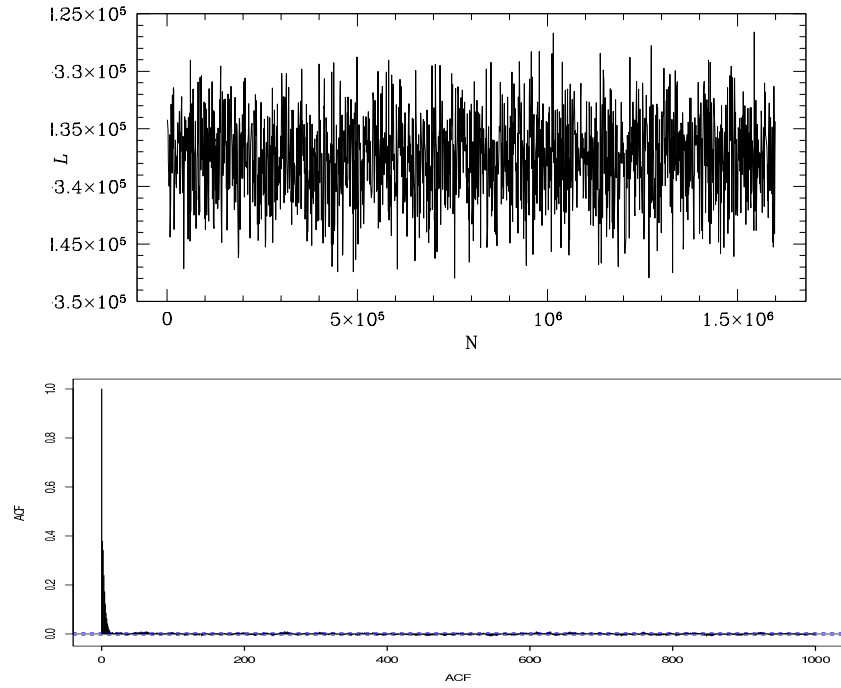


FIG 4. Upper: The trace of the likelihood from a chain run with data D_1 . Lower: The ACF plot using this MCMC chain.

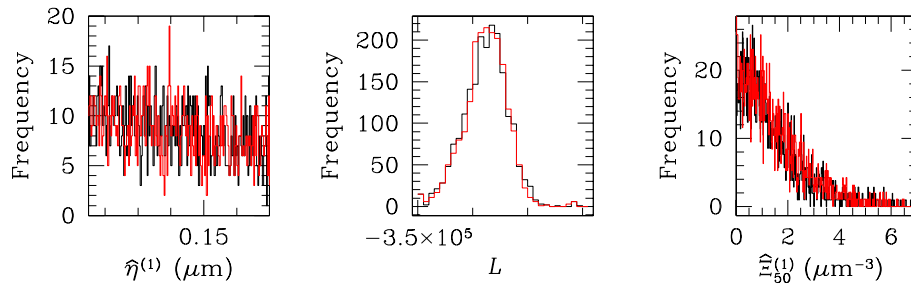


FIG 5. The histograms of the learnt material density in the voxel marked by the beam location index $i = 50$ and the smallest beam energy, ($k = 1$), from two disjoint parts (middle and end) of the MCMC chain that is 1.6×10^6 steps long, are depicted in red and black respectively, in the right panel. The histograms of the learnt correction function for $k = 1$, obtained for these two parts of the chain are displayed in the left panel. The histograms of the value of the likelihood in these two parts of the chain are plotted in red and black in the middle panel. The chain was run with real image data D_1 .

a chosen luminosity density function is then advanced as a model for the density. We advance a methodology that is an improvement upon this. One key advantage of our approach is that estimates of the 3-D material density function are derived from non-invasive and nondestructive bulk imaging techniques. This feature sets our approach beyond standard methodology that typically relies on experimental designs involving the etching away of layers of the sample material at specific depths. Though the microstructure, at this depth, can in principle be identified this way, a measure of $\rho(\mathbf{x})$ is not achievable. That too, only constraints on the microstructure at such specific depths are possible this way, and interpolation between the layers - based on assumptions about the linearity of the microstructure distribution - are questionable in complex real-life material samples. Of course, such a procedure also damages the sample in the process. Thus, the scope of the methodology that we advance is superior.

As far as the methodology is concerned, to begin with, given one observed image of the system, the problem discussed above is ill-posed; the two obvious remedies that are then invoked include the expansion of the information domain and the identification of strong priors on $\rho(\mathbf{x})$ and $\eta(z)$. Strong priors exist in the microscopy literature, for the shape of the blurring or correction function $\eta(z)$. Thus, elicitation using existing literature is what we fall back on to gather the prior probability distribution of $\eta(z)$. In particular, there is deterministic information available in the literature about $\Phi(0)$, allowing for identifiability of the global scales of the unknown material density and correction function. In our discretised model, the ratio of known to unknown parameters typically varies from 0.96 to about 0.99, for the non-parametric and semi-parametric models for $\eta(z)$ respectively. On the other hand, the identification of the geometric priors on $\rho(\mathbf{x})$ does not come from the literature but are a bespoke feature of the model, developed in the context of this application after examination of the operator $\langle \mathcal{P}(\cdot) \rangle$ that maps $\rho(\mathbf{x}) * \eta(z)$ to the image space.

The expansion of the information domain that we hinted at above, is made possible in this work by suggesting multiple images of the same material sample taken with electron beams of different energies. Given the differential penetration depths of beams of different energies, the images taken in this way are realisations of the 3-D structure of the material sample to different depths. While a number of attempts that use multiple viewing angles have been reported in the literature, (...) the imaging of the system at different energies is less common. A logistical advantage of imaging the sample at different energies exists over imaging at different viewing angles. Firstly, the precision level required in the angle measurement in the latter experiment is difficult to achieve. Besides, in Scanning Electron Microscopes, the viewing angle is varied by re-mounting the sample on a stub that is differently inclined to the electron beam than what the sample was mounted on before. This is relatively more disadvantageous than the method suggested in the paper in the sense that mounting and remounting of the sample allows image data at only a few, pre-specified viewing angles, on the basis of which 3-D material density reconstruction has to be performed.

An important point to make is that $\eta(z)$ is the blurring function in our model though it is not the ρz correction that is used in Microscopy literature to suggest the correction; the connection between the two is discussed in Section 4.3.

When the parameters are such that $R0^{(k)} \leq \delta$ for $k \leq k_{in}$, $k_{in} \leq N_{eng}$ - as in the case of images taken in X-rays - isotropy is guaranteed for the density structure within all interaction-volume at energies $E \leq \epsilon_{k_{in}}$, so that the spatial averaging is the easiest for $k \leq k_{in}$; it involves just the integral over R . This is what renders models with $k_{in} = N_{eng}$ easiest. When $k_{in} < N_{eng}$ the models are one step higher in the complexity hierarchy of our three models. Then we use a simple construct from spatial statistics, namely nearest neighbour averaging, to approximate the density at a given $R > R0^{(k_{in})}$. The effect of this construct can be seen as inducing local isotropy in the density field.

We model the morphology as a hemisphere, centred at the point of beam incidence, of radius $R0^{(k)}$, given the beam energy ϵ_k , $k = 1, \dots, N_{eng}$. Though for some high atomic number metals such a hemi-spherical shape for the interaction volume is supported by simulations of material samples, for lower atomic number materials, this shape typically deviates from sphericity, with a marked pinching close to the surface (Goldstein et al. 2003). If the results of such simulations are available, the morphology of the “interaction volume” can be approximated. In this context, a crucial point to make is that such simulations rely on the knowledge of the material density function - the Z -distribution of the material particles is however unknown in real-life material samples, leading to a motivation for a modular density reconstruction methodology⁵. Thus, to keep our methodology modular, we chose to work with a model that assumes the morphology of the interaction-volume, while ensuring that errors - if any - induced by such a model assumption are taken account of, and effects of the same are compensated for, in the subsequent modelling process. The consequence of this model assumption is in fact the over-estimation of the size of the interaction-volume at low z . It is to be noted that within our simplified model for the shape of the interaction-volume, the very estimation of $R0^{(k)}$ using the work by Kanaya and Okamaya might be considered an overestimation, see Goldstein et al. (2003).

Thus, we worry if the considered model for the size and shape of the interaction-volume, biases our estimate of the unknowns. Our over-estimation of the size of the interaction-volume implies that for a given material and given image type, the number of voxels lying wholly inside the interaction-volume could be overestimated. If this is the case, the only disadvantage will be that we might be applying the model of a higher level of complexity to a sample, for which a simpler model is sufficient. However, for all models, the problem has been shown to be well-posed if the blurring function is assumed known, but underdetermined otherwise, though for the simplest model, the problem is defined by less number of degrees of freedom. For all models, the quantification of deviation from uniqueness is understood.

A point worth noting is that the deviation from uniqueness in the estimation of the two unknown functions are approximately linear (Equation 4.27), though in opposing directions. Thus, we see in Figure 5 of the supplementary material, that for a choice of simulated image data, the estimate of the correction function is improved in the case of implementation of the semi-parametric model of $\eta(z)$ over the non-parametric one; correspondingly, the estimate of the density function is improved in the former implementation.

⁵For a given simulation of the interaction-volume of a given alloy sample, we attempted the estimation of the constant material density contours using a 3-parameter non-linear regression model.

The method that we have discussed above is indeed developed to solve an unconventionally difficult deconvolution problem, but the method is equally capable of estimating the unknown density in an integral equation of the 1st kind - Fredholm or Volterra - and thereby be applied towards non-parametric density reconstruction in a wide variety of contexts, when image synthesis is possible.

7. Summary and Conclusions. In this work we have advanced a Bayesian methodology that performs non-parametric reconstruction of the material density and a non-parametric or semi-parametric reconstruction of the blurring function, given 2-D images of the system taken in any kind of radiation that is generated in the bulk of the material sample, due to atomistic interactions between the material molecules and an electron beam that is injected into it. This methodology is advanced as capable of estimating the unknown functions even when the the inverse Radon transform is not stable - material density function is heterogeneous, the density field is not necessarily convex, and is marked by a dense or sparse modal structure characterised by abruptly declining modal strengths. A mixture model is also not satisfactory in this situation. This inverse problem, when cast as an integral equation, connects the measured 2-D radiation in any pixel with multiple integrations over the convolution of an unknown density and an unknown correction function. The novelty of our proposal of a solution to this harder-than-usual inverse problem includes the imaging of the system at distinct beam energies, adoption of a fully discretised model, identifying geometric priors on the density and borrowing existing knowledge of correction function shapes from the microscopy literature.

The posterior of the model given the image data is shown to reduce to a product over a series of Dirac measures that are centred at the solution of the equation $\tilde{I}_i^{(k)} = I_i^{(k)}$, where $I_i^{(k)}$ is the result of $\mathcal{P}(\rho(\mathbf{x}) * \eta(z))$ over the ik -th interaction volume, $\forall i = 1, \dots, N_{data}, k = 1, \dots, N_{eng}$. The non-uniqueness in the estimate of the density function is shown to be linearly dependent, but of the opposite nature, to the non-uniqueness in the correction function. Also, the deviation from uniqueness in the estimate of the density in a voxel that is more densely packed than another, is comparatively less.

We sample from our high-dimensional posterior using adaptive Metropolis-Hastings. We implement a dual-block update, first over the density and then over the correction function. In the random-walk implementation that we adopt, the dispersion of the proposal density is set as the empirical dispersion over the last chosen number of steps. The mean and covariance structures of the proposal density of $\eta(z)$ are not independent but enjoy a constraint from the knowledge of the value of $\Phi(0)$, as given by microscopic theory.

With the stability of the solutions and the deviations from uniqueness discussed, the method is advanced as a modular solution for the problem at hand. The scope of such applications is of course ample, including the identification and quantification of the density of the metallic molecules that have infused into a piece of polymer that is employed for charge storage purposes, degrading the quality of the device as a result, or the learning of the density of a heterogeneous nanostructure leading to increased understanding of lack of robustness of device behaviour, or identification of the distribution of multiple phases of an alloy in the depth of a metallic sample meant to be used in industry and possibly even estimation of density of luminous matter in astronomical objects, viewed with telescopes at different wavelengths. In

fact, in the case of self-emitting systems that are studied in the emitted particles, the problem is simpler, (as in several other applications), since the interaction-volume is not relevant and the integral reduces to the (easier in general) Volterra integral equation of the first kind. In either case, domain-specific details need to be invoked to attain dimensionality reduction.

APPENDIX A: NON-PARAMETRIC MODEL FOR CORRECTION FUNCTION

The under-determinedness of the problem is checked by motivating the density of the prior probability measure on $\eta(z)$ using the known shape of the correction as given in microscopy theory, i.e. the shape of $\Psi(\rho z) \exp(-cz)$, where the material-dependent constant $C \in \mathbb{R}$ is physically speaking, determined by the linear absorption coefficient in case of X-rays and by BSE coefficients in the case a BSE image is considered. A uniform prior is assigned to C , with $\pi(C) = \mathcal{U}[10^{-4}, 10^{-2}]$ when the BSE image is the data, otherwise, for the X-ray image, $\pi(C) = \mathcal{U}[10^{-4}, 10^{-2}]$, where c is measured in units of μm . These are the expected ranges for C (Goldstein et. al 2003, <http://physics.nist.gov/PhysRefData/XrayMassCoef/tab3.html>), given the beam energies (~ 10 kV) and materials that we work with. $\Psi(\rho z)$ resembles a 2-parameter folded normal distribution $\mathcal{N}_F(\eta_0, S)$, with parameters $\eta_0, S \in \mathbb{R}$; $\eta_0, S > 0$.

In the non-parametric model for the correction function, we choose folded normal priors for $\eta(z)$, i.e. $\pi(\eta) = \mathcal{N}_F(\eta|\eta_0, S)$. Also, microscopy theory allows for $\Psi(0)$ to be known deterministically. Then setting $\pi(\eta^{(1)}) = 1$, we relate η_0, S and $\Psi(0)$. This relation is used to compute s , while a uniform prior is assigned to the hyperparameter η_0 . Thus, this is a non-parametric model of $\eta(z)$.

The correction function learnt at any iteration is normalised by the factor of $\hat{\eta}^{(1)}/\Psi(0)$, where $\hat{\eta}^{(1)}$ is the estimated unscaled correction function in the first Z -bin.

APPENDIX B: SEMI-PARAMETRIC MODEL FOR CORRECTION FUNCTION

On other occasions, we model $\eta(z)$ differently. We approximate the form of $\eta(z)$ by the shape of $\Psi(\rho z) \exp(-cz)$ - as suggested in the microscopy literature - multiplied by the scale-factor Q , where $Q \in \mathbb{R}$. Also, in the beam energies that we are working at, mass absorption coefficients of most materials are such that $C \lesssim 10^{-2}$, so that $\exp(-cz) \approx 1$. Thus, we approximate further to suggest that $\eta(z)$ resembles a folded normal distribution in shape. Under this model assumption the scaling for $\eta(z)$ is the Z -independent constant Q and we represent $\eta(z)$ as

$$(B.1) \quad \eta(z) \equiv Q \left[\exp\left(-\frac{(z - \eta_0)^2}{2s^2}\right) + \exp\left(-\frac{(z + \eta_0)^2}{2s^2}\right) \right]$$

Thus, in this model, $\eta(z)$ is deterministically known if the parameters Q, η_0 and S are, where, $\eta_0 \in \mathbb{R}$ and $S \in \mathbb{R}$ are the mean and dispersion that define the folded normal distribution. Out of these three parameters, only two are independent since $\Psi(0)$ is known (see Section A). Thus, by setting $\psi(0) = 2Q \exp[-\eta_0^2/2s^2]$, we relate η_0 deterministically to s and Q . In this model of the blurring function, we put Gaussian priors on Q and s and we calculate η_0 . Thus, this model of the

correction function is semi-parametric in the sense that $\eta(z)$ is parametrised though the parameters involved in the model are non-parametrically reconstructed. We illustrate the effects of both modelling strategies in Section 6 of the Supplementary materials.

APPENDIX C: UPDATING DETAILS

For the n -th iteration, $n = 1, \dots, N_{burnin}, \dots, N_{max}$, the state vector $\varepsilon_n = (\varepsilon_n^\Xi, \varepsilon_n^\Phi)$, where $\varepsilon_{n+1}^\Xi = \{\Xi_i^{(1)}|_{n+1}, \dots, \Xi_{N_{data}}^{(N_{eng})}|_{n+1}\}$ and $\varepsilon_{n+1}^\Phi = \{\Phi^{(1)}|_{n+1}, \dots, \Phi^{(N_{eng})}|_{n+1}\}$ and the proposed blocks are given by $\tilde{\varepsilon}_n^\Xi = \{\tilde{\Xi}_i^{(1)}, \dots, \tilde{\Xi}_{N_{data}}^{(N_{eng})}\}$ and $\tilde{\varepsilon}_n^\Phi = \{\tilde{\Phi}^{(1)}, \dots, \tilde{\Phi}^{(N_{eng})}\}$. The updating is performed as follows.

1. Define $\varepsilon_0 = (\varepsilon_0^\Xi, \varepsilon_0^\Phi)$.
2. At the $n + 1$ -th iteration,

$$(C.1) \quad \begin{aligned} \varepsilon_{n+1}^\Xi &= \tilde{\varepsilon}_{n+1}^\Xi && \text{with probability } v(\varepsilon_n^\Xi, \tilde{\varepsilon}_n^\Xi | \varepsilon_n^\Phi) \\ \varepsilon_{n+1}^\Xi &= \varepsilon_n^\Xi && \text{with probability } 1 - v(\varepsilon_n^\Xi, \tilde{\varepsilon}_n^\Xi | \varepsilon_n^\Phi) \end{aligned}$$

where

$$(C.2) \quad v(\varepsilon_n^\Xi, \tilde{\varepsilon}_n^\Xi | \varepsilon_n^\Phi) = \min \left(1, \frac{\pi(\tilde{\varepsilon}_n^\Xi, \varepsilon_n^\Phi | \mathcal{I}) q(\tilde{\varepsilon}_n^\Xi, \varepsilon_n^\Xi | \varepsilon_n^\Phi)}{\pi(\varepsilon_n^\Xi, \varepsilon_n^\Phi | \mathcal{I}) q(\varepsilon_n^\Xi, \tilde{\varepsilon}_n^\Xi | \varepsilon_n^\Phi)} \right).$$

Here $\mathcal{I} := \{I_1^{(1)}, \dots, I_{N_{data}}^{N_{eng}}\}$ and

$$(C.3) \quad \tilde{\varepsilon}_n^\Xi \sim q(\varepsilon_n^\Xi, \tilde{\varepsilon}_n^\Xi | \varepsilon_n^\Phi).$$

The proposal density for any element of the $\tilde{\varepsilon}_n^\Xi$ vector is folded-normal in shape, conditioned on the previous value of this element; the dispersion of this proposal density is given by the empirical dispersion of all previous values since $n = n_0$. Thus, this proposal density is independent of ε_n^Φ for all n , by choice.

- 3.

$$(C.4) \quad \begin{aligned} \varepsilon_{n+1}^\Phi &= \tilde{\varepsilon}_n^\Phi && \text{with probability } v(\varepsilon_n^\Phi, \tilde{\varepsilon}_n^\Phi | \varepsilon_{n+1}^\Xi) \\ \varepsilon_{n+1}^\Phi &= \varepsilon_n^\Phi && \text{with probability } 1 - v(\varepsilon_n^\Phi, \tilde{\varepsilon}_n^\Phi | \varepsilon_{n+1}^\Xi) \end{aligned}$$

where

$$(C.5) \quad v(\varepsilon_n^\Phi, \tilde{\varepsilon}_n^\Phi | \varepsilon_{n+1}^\Xi) = \min \left(1, \frac{\pi(\varepsilon_{n+1}^\Xi, \tilde{\varepsilon}_n^\Phi | \mathcal{I}) q(\tilde{\varepsilon}_n^\Phi, \varepsilon_n^\Phi | \varepsilon_{n+1}^\Xi)}{\pi(\varepsilon_{n+1}^\Xi, \varepsilon_n^\Phi | \mathcal{I}) q(\varepsilon_n^\Phi, \tilde{\varepsilon}_n^\Phi | \varepsilon_{n+1}^\Xi)} \right).$$

where $\tilde{\varepsilon}_n^\Phi \sim q(\varepsilon_n^\Phi, \tilde{\varepsilon}_n^\Phi | \varepsilon_{n+1}^\Xi)$.

4. Then $\varepsilon_{n+1} = \{\varepsilon_{n+1}^\Xi, \varepsilon_{n+1}^\Phi\}$. We return ε_{n+1} , $\forall n > N_{burnin}$. Repeat for all $n = 1, \dots, N_{burnin}, \dots, N_{max}$.

SUPPLEMENTARY MATERIAL

Supplement A: Supplementary Material for “A Bayesian learning of material density and the blurring function, given 2-D images taken with bulk Microscopy techniques”

(). The attached supplementary material consists of a brief discussion about the relative complexity of the three models that have been advanced for the three resolution regimes of the imaging techniques that we consider in the paper. A section on the analysis of simulated image data forms the latter part of the supplementary section.

ACKNOWLEDGMENTS

We are thankful to Dr. John Aston, Dr. Sourabh Bhattacharya and Prof. Jim Smith for their helpful suggestions. DC acknowledges the Warwick Centre for Analytical Sciences fellowship.

REFERENCES

- Arridge, S. R., & Schotland, J. C. (2009), “Optical tomography: forward and inverse problems,” *Inverse Problems*, 25, 123010.
- Bertero, M., & Boccacci, P. (1998), *Introduction to inverse problems in imaging*, : Taylor and Francis.
- Chakrabarty, D. (2010), “Non-parametric deprojection of surface brightness profiles of galaxies in generalised geometries,” *Astronomy & Astrophysics*, 510, A45+.
- Chib, S., & Greenberg, E. (1995), “Understanding the Metropolis-Hastings Algorithm,” *The American Statistician*, 49(4), 327.
- Cotter, S., Dashti, M., & Stuart, A. (2010), “Approximation of Bayesian Inverse Problems,” *SIAM Journal of Numerical Analysis*, 48, 322–345.
- Davis, G. R., Dowker, S. E. P., Elliott, J. C., Anderson, P., Wassif, H. S., Boyde, A., Goodship, A. E., Stock, S. R., & Ignatiev, K. (2002), “Non-destructive 3D structural studies by X-ray microtomography,” *Advances in X-ray Analysis*, 45, 485.
- Donoho, D., & Tanner, J. (2005), “Sparse Nonnegative Solutions of Underdetermined Linear Equations by Linear Programming,” *Proceedings of the National Academy of Sciences*, 102(27), 9446.
- Dorn, O., Bertete-Aguirre, H., & Papanicolaou, G. (2008), “Adjoint fields and sensitivities for 3D electromagnetic imaging in isotropic and anisotropic media,” *Inverse Problem and Imaging*, 1943, 35.
- Erlandsen, S., Macechko, P. T., & Frethem, C. (1999), “High resolution backscatter electron (BSE) imaging of immunogold with in-lens and below-the-lens field emission Scanning Electron Microscopes,” *Scanning Microscopy*, 13(1), 43.
- Gilks, W. R., & Roberts, G. O. (1996), Strategies for improving MCMC., in *Markov Chain Monte Carlo in Practice*, eds. W. Gilks, S. Richardson, & D. Spiegelhalter, Interdisciplinary Statistics, Chapman and Hall, London, pp. 89–114.
- Goldstein, J., Newbury, D. E., Joy, D. C., Lyman, C. E., Echlin, P., Lifshin, E., Sawyer, L., & Michael, J. (2003), *Scanning Electron Microscopy and X-ray Microanalysis*, New York: Springer Science+Business Media.
- Haario, H., Laine, M., Mira, A., & Saksman, E. (2006), “DRAM: Efficient adaptive MCMC,” *Statistics and Computing*, 16, 339.
- Hans, C. (2009), “Bayesian lasso regularisation,” *Biometrika*, 96(4), 835.
- Heinrich, K. F. J., & Newbury, D. E. (1991), *Electron probe quantitation*, New York: Springer.
- Helgason, S. (1999), *The Radon transform*, Progress in Mathematics, Boston: Birkhauser.
- Joly-Puttez, L. (2011), Tribology of Nanoparticles., in *Handbook of Nanohysics, Nanoparticles and Quantum Dots*, ed. e. K. D. Sattler, CRC Press, Taylor and Francis, pp. 26–1.
- Kanaya, K., & Okamaya, S. (1972)*Jl. of Physics D., Applied Physics*, 5, 43.

- Kutchment, P. (2006), Generalised Transforms of the Radon Type and their Applications., in *The Radon Transform, Inverse Problems, and Tomography*, eds. G. Olafsson, & e. E. T. Quinto, Vol. 63, American Mathematical society, p. 67.
- Lee, R. E. (1993), *Scanning electron microscopy and X-ray microanalysis*, New Jersey, USA: Prentice-Hall.
- Leone, F., Nottingham, R. B., & Nelson, L. S. (1961), "The Folded Normal Distribution," *Technometrics*, 3(4), 543.
- Li, L., & Speed, T. (2000), "Parametric deconvolution of positive spike trains," *Annals of Statistics*, 28, 1270.
- Markoe, A., & Quinto, E. T. (1985), "An Elementary Proof of Local Invertibility for Generalized and Attenuated Radon Transforms," *SIAM J. Math. Anal.*, 16, 1114.
- Merlet., C. (1994), "An Accurate Computer Correction Program for Quantitative Electron Probe Microanalysis," *Mikrochim. Acta*, 114/115, 363.
- Natterer, F., & Wbbeling, F. (2001), *Mathematical methods in image reconstruction*, Philadelphia: SIAM.
- Panaretos, V. M. (2009), "On Random Tomography with Unobservable Projection Angles," *Annals of Statistics*, 37(6), 3272.
- Park, J. M., Kim, K. B., Kim, D. H., Mattern, N., Li, R., Liu, G., & Eckert, J. (2010), "Multi-phase Al-based ultrafine composite with multi-scale microstructure," *Intermetallics*, 18(10), 1829.
- Park, T., & Casella, G. (2008), "The bayesian lasso," *Journal of the American Statistical Association*, 482, 681.
- Pouchou, J. L., & Pichoir, F. (1984), *PAP (ρZ) procedure for improved quantitative microanalysis*, Microbeam Analysis, ed. J.T.Armstrong, San Francisco, California: San Francisco Press.
- Reed, S. J. B. (2005), *Electron Microprobe Analysis and Scanning Electron Microscopy in Geology*, Cambridge: Cambridge University Press.
- Rullgrd, H. (2004), "Stability of the inverse problem for the attenuated Radon transform with 180 data," *Inverse Problems*, 20, 781.
- Stuart, A. (2010), "Inverse problems: a Bayesian perspective," in *Acta Numerica*, Vol. 19 Cambridge University Press, p. 451.
- Tarantola, A. (2004), *Inverse Problem Theory and Methods for Model Parameter Estimation*, Philadelphia: SIAM.
- Tibshirani, R. (1996), "Regression shrinkage and selection via the lasso," *Journal of the Royal Statistical Society, Series B*, 58(1), 267.
- Tricomi, F. G. (1985), *Integral Equations*, New York: Dover Publications.
- Wong, F. S. L., & Elliott, J. C. (1997), "Theoretical Explanation of the Relationship between Backscattered Electron and X-Ray Linear Attenuation Coefficients in Calcified Tissues," *Scanning*, 19, 541.
- Wright, J., Yang, A., Ganesh, A., Sastry, S., & Ma, Y. (2009), "Robust Face Recognition via Sparse Representation, and its online supplementary material," *IEEE Transactions on Pattern Analysis and Machine Intelligence (PAMI)*, 31(2).
- Yamasaki, M., Hashimoto, K., Hagihara, K., & Kawamura, Y. (2010), "Multimodal Microstructure Evolution in Wrought Mg-Zn-Y Alloys with High Strength and Increased Ductility," *Materials Science Forum*, 654-656, 615.

DEPARTMENT OF STATISTICS
UNIVERSITY OF WARWICK
COVENTRY CV4 7AL, U.K.
E-MAIL: d.chakrabarty@warwick.ac.uk
E-MAIL: r.beanland@warwick.co.uk

EMERGING TECHNOLOGY RESEARCH CENTRE
DEMONTFORT UNIVERSITY
HAWTHORN BUILDING, THE GATEWAY
LEICESTER, LE1 9BH
U.K.
spaul@dmu.ac.uk
nare.gabrielyan@email.dmu.ac.uk

NOVARTIS VACCINES AND DIAGNOSTICS
VIA FIORENTINA 1, SIENA, ITALY
fabio.rigat@novartis.com

SUPPLEMENTARY MATERIAL FOR “A BAYESIAN LEARNING OF MATERIAL DENSITY AND THE BLURRING FUNCTION, GIVEN 2-D IMAGES TAKEN WITH BULK MICROSCOPY TECHNIQUES”

BY DALIA CHAKRABARTY, FABIO RIGAT, NARE GABRIELIAN, RICHARD BEANLAND AND SHASHI PAUL

1. Hierarchical complexity in the models. The model corresponding to the analysis of the SEM images is the most complex of our three models because in this model, the number of parameters involved in the estimation of any unknown, say $\Xi_i^{(k)}$, is the highest, $i = 1, \dots, N_{data}$, $k = 1, \dots, N_{eng}$ - the number of other voxels inside the ik -th interaction-volume, in addition to the unknown correction function parameters. In contrast to this, in the simpler two models, (high or low- \mathcal{Z} material samples imaged in X-rays), the estimation of any $\Xi_i^{(k)}$ involves a comparatively smaller number of unknown parameters. Thus, for the same ratio of the number of unknown parameters and equations, inference is harder in the 3rd model, compared to in the other two models.

In fact, for this simplest of the 3 models, there is an additional constraint on the density field, linking density estimates in voxels at a given value of the beam energy index. We see that at any $k \in \{1, \dots, N_{eng}\}$, $[\tilde{I}_i^{(k)} - \tilde{I}_i^{(k-1)}]/[\tilde{I}_j^{(k)} - \tilde{I}_j^{(k-1)}] = \Xi_i^{(k)}/\Xi_j^{(k)}$, $\forall i, j = 1, \dots, N_{data}$. Thus, for any beam-energy index k , if $\tilde{I}_i^{(k)} - \tilde{I}_i^{(k-1)} = 0$, it implies that the density $\{\Xi_m^{(k)}\}_{m=1}^{N_{data}} = 0$. This effectively constrains the density field. Thus, for an underlying density that is sparser in its native space than another, the estimation is better constrained. With the semi-parametric model for the correction function, even when the unknown (test) density is dense, its estimation is shown to be well constrained (see Figure 5).

This discussion on uniqueness of the solution implies that the learnt density, given a known correction function, is unique, irrespective of how sparse or dense the unknown density is in its native space, and also independent of the complexity of our model, (i.e. the easiest, the second hardest or the hardest of the three of our models); this owes to our expanding the information domain. However, the individual estimation of $\rho(\mathbf{x})$ as well as $\Phi(z)$ renders the problem underdetermined. Unlike in some other underdetermined problems in which we can estimate one subset of the unknown parameters without uncertainty and the uncertainty accompanies only the estimation of the other parameters, this is not possible in our case, since estimates of $\{\Phi^{(1)}, \dots, \Phi^{(N_{eng})}\}$ and $\{\Xi_1^{(1)}, \dots, \Xi_{N_{data}}^{(N_{eng})}\}$ are sought within our model in a product form. However, we show above that the non-uniqueness in the estimation of $\{\Phi^{(1)}, \dots, \Phi^{(N_{eng})}\}$ determines the non-uniqueness in the estimate of $\Xi_1^{(1)}, \dots, \Xi_{N_{data}}^{(N_{eng})}$. In particular, when the semi-parametric model for $\eta(z)$ is implemented, the non-uniqueness in the estimation of $\{\Phi^{(1)}, \dots, \Phi^{(N_{eng})}\}$ is low, implying low levels of non-uniqueness in the estimation of the density.

2. Some illustrations on simulated data. We describe the application of the inverse methodology described above to simulated images in order to test of the

method, i.e. compare the true density $\rho(\mathbf{x})$ and true correction function $\eta(z)$ with the estimated density and correction function - $\hat{\rho}(\mathbf{x})$ and $\hat{\eta}(z)$ respectively.

The discussed examples include simulations of Copper-Tungsten alloys, i.e. example of high- \mathcal{Z} material, the true density function is dense (Sample I-CuW), the same material sample marked by the sparse density structure characterised by isolated modes with sharp edges, (Sample II-CuW) and simulated dense and sparse density samples of a Ni-Al alloy which is a low- \mathcal{Z} material, i.e. Sample I-NiAl and Sample II-NiAl respectively.

The strengths of any two modes in either sample are not necessarily distinguishable. Given the sharp density contrasts along the edges of the modes, neither the isolated modal material density structure nor the longitudinal growths of overdensity in the same, in our simulated samples can be satisfactorily modelled with a Gaussian mixture model.

The (simulated) images are produced at 18 or 10 different beam energy values, corresponding to $\epsilon_k=2+k$ kV, $k = 1, \dots, N_{eng}$. We work with $N_{data}=225$. For the low resolution imaging techniques, $\delta=1.33 \mu\text{m}$ while for the illustration of the high resolution technique (such as SEM), a resolution of $\delta=9$ nm, is considered. For each k , the image representing the 2-D densities in 225 pixels, arranged in a 15×15 square array, is computed from the true density and true correction function which are chosen as follows:

$$(2.1) \quad \rho(x, y, z)|i = \Upsilon \frac{A_i}{\left[\epsilon^2 + \frac{x^2}{B_i^2} + \frac{y^2}{B_i^2} + \frac{z^2}{B_i^2(1-Q_i^2)} \right]} \quad \text{where}$$

$\Upsilon = (\text{int})(N_{eng}U_1)$, $U_1 \sim \mathcal{U}[0, 1]$ for Sample II and Sample III, $\Upsilon = 1$ for Sample I, $A_i = U_2^2$, $U_2 \sim \mathcal{U}[0, 1]$, $B_i = U_3$, $U_3 \sim \mathcal{U}[0, n\delta]$ $n \in \mathbb{Z}^+$, $Q_i = U_4$, $U_4 \sim \mathcal{U}[0, 1]a : \forall i = 1, \dots, N_{data}$. Here $\mathcal{U}[0, q]$ is the uniform distribution over the range $[0, q]$, $q \in \mathbb{R}$. The true correction function is chosen to emulate a folded normal distribution with values of mean γ and dispersion θ .

$$(2.2) \quad \eta(z) = \exp \left[\frac{(z - \gamma)^2}{2\theta^2} \right] + \exp \left[\frac{(z + \gamma)^2}{2\theta^2} \right]$$

The true density and correction function are then used in Equation 2.1 of the main text to generate the radially averaged projection of the convolution of $\rho(\mathbf{x})$ and $\eta(z)$, for the k^{th} value of E , giving rise to N_{eng} images. These comprise the simulated data for the methodology described above.

We start MCMC chains, starting with a seed density in the ik^{th} voxel defined as $\tilde{I}_i^{(k)}/\Phi_{seed}^{(k)}$, where the starting blurring function $\{\eta_{seed}^{(k)}\}_{k=1}^{N_{eng}}$ helps define $\Phi_{seed}^{(k)} = \sum_{j=1}^k \eta_{seed}^{(j)}(h^{(j)} - h^{(j-1)})$. The initial guess for the correction function is chosen to be motivated by the forms suggested in the literature; in fact, we choose the initial correction function to be described by a half-normal distribution, with a standard deviation of $5\mu\text{m}$ and mean of $5\mu\text{m}$. The simulated images are produced with $\sigma_i^{(k)}=0.05$ to $.005$ times $\tilde{I}_i^{(k)}$. We use adaptive Metropolis Hastings for our inference, (Haario et al. 2006).

2.1. *Low resolution, high- \mathcal{Z} material.* These illustrations are performed with intrinsic densities that are sparse (Sample II-CuW) and dense (Sample I-CuW). The

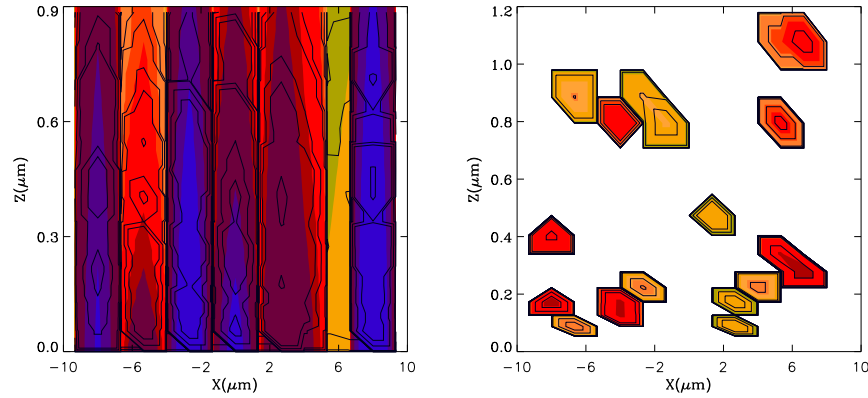


FIG 1. Estimated material density $\hat{\rho}(x, y, z)$ overplotted in the $X - Z$ plane, $\forall y$, in solid contour lines, on the true density (in filled coloured contours), given simulated images of Copper-Tungsten alloy - Sample I-CuW (left) and Sample II-CuW (right). The simulated image data corresponds to a low-resolution imaging technique (such as when the system is imaged by an SEM in X-rays), at different beam energy values. The material density estimate at the modal level of the posterior probability is plotted. The semi-parametric model for the correction function was used for these runs.

idea behind the modelling in this case is that the radial extent of the interaction-volume corresponding to $E = \epsilon_{N_{eng}}$, is less than the cross-sectional area of the voxel on the $Z=0$ surface, rendering the modelling the simplest out of the three illustrations we discuss. The resolution of this imaging technique allows for 15 beam pointings over an interval of $20 \mu\text{m}$, from $X=-10\mu\text{m}$ to $X=10\mu\text{m}$ at given Y , at a spatial resolution of $\delta=1.33 \mu\text{m}$, and then at intervals of δ from $Y=-10\mu\text{m}$ to $Y=10\mu\text{m}$. We implement these test data, both when we consider a fully non-parametric model for $\eta(z)$ as well as the semi-parametric model.

Figure 1 represents the estimated density functions for the two simulated samples, represented as contour plots in the $X - Z$ plane, $\forall Y = y$, superimposed over the respective true densities which are shown as filled contour plots, when the semi-parametric model for $\eta(z)$ is used, for $\sigma_i^{(k)} = 0.05\tilde{I}_i^{(k)}$. Figure 2 represents results of implementation of the non-parametric models for $\eta(z)$, using $\sigma_i^{(k)} = 0.01\tilde{I}_i^{(k)}$. It includes the profile of $I_i^{(k)}$ as a function of $\lambda(i) = i \bmod \sqrt{N_{data}}$, $\lambda : \mathbb{Z}_+ \rightarrow \mathbb{Z}_+$, i.e. the pixel number along the X or Y axes, over all $k = 1, \dots, N_{eng}$ with Z for all x and y , compared to the profile of the true density. Similarly, the estimated $\hat{\eta}(z)$ and true correction function are also compared. Trace plots for the chains are also depicted.

It is to be noted that the definition of the likelihood in terms of the mismatch between data and $\mathcal{P}(\hat{\rho} * \hat{\eta})$ compels $\mathcal{P}(\hat{\rho} * \hat{\eta})$ and \tilde{I} to coincide, even if $\hat{\rho}(\mathbf{x})$ is poorly estimated, though the superposition of the profiles of $\mathcal{P}(\hat{\rho} * \hat{\eta})$ with E and the data serves as a zeroth order check on the functioning of the involved coding.

2.2. Low resolution, low- Z material. Distinguished from the last section, in this section we deal with the case of a low atomic number material imaged at coarse imaging resolution. In this case, the radial extent of the interaction-volume exceeds the size δ of a voxel on the $Z=0$ plane for $\epsilon_k > \epsilon_{k_{in}}$, for $k = 1, \dots, k_{in}, \dots, N_{eng}$. The illustration of this case is discussed here for a low- Z Sample II-NiAl, that is an

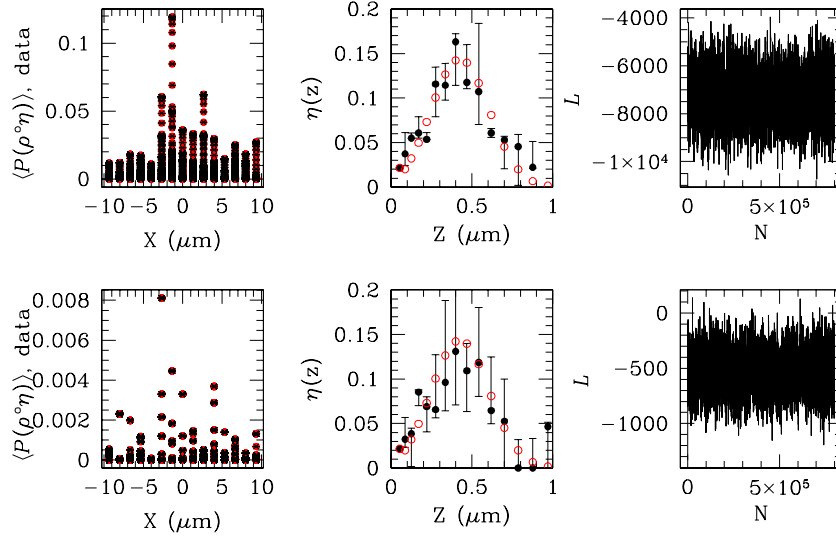


FIG 2. Left: - Spatially averaged projection of $\hat{\rho} * \hat{\eta}$ plotted in black, in model units, as a function of $\lambda(i) = i \text{ modulo } \sqrt{N_{\text{data}}}$, (where the beam location index $i = 1, \dots, N_{\text{data}}$, $N_{\text{data}} = 225$), over the data (in red), for all beam energy values ϵ_k , $k = 1, \dots, 18$, for Sample I-CuW (upper panel) and Sample II-CuW (lower). The estimated correction function is shown in the middle panels, in black, superimposed on the true $\eta(z)$ for the two samples (in red). The error bars in the above plots, as well as in all plots that follow, correspond to 95% highest probability density credible regions, while the modal level of the posterior is marked by a symbol (filled circle above). The likelihood trace from the MCMC chains is shown in the right panels. The fully non-parametric model for the correction function was implemented.

allow of Nickel, Aluminium, Tallium, Rhenium; see DSouza, Beanland, Hayward & Dong (2011). All other details are as in the previous illustration.

Figure 3 is used to describe the learnt density structure; visualisation to this effect is provided for the N-Al alloy sample in terms of the plots of $\hat{\rho}(\mathbf{x})$ against Z , at chosen values of X and Y inside the sample. Since there are 225 voxels used in these exercises, the depiction of the density at each of these voxels is judged beyond room in the paper, but the density structure is scanned across all voxels distinguished by the 15 X coordinate values, at one high, and one low value of the voxel Y coordinate in the respective figures.

2.3. High resolution. Distinguished from the last section, in this section we deal with the case of simulated Sample I-NiAl and Sample II-NiAl, imaged at coarse imaging resolution. In this case, the interaction-volume over which the convolution of the unknown functions $\rho(\mathbf{x})$ and $\eta(z)$ is averaged and projected, given a beam-energy, exceeds the volume of the voxel set by the resolution of the imaging technique at hand (imaged in BSE), at this given energy.

The challenge posed by the high resolution ($\lesssim 10$ nm) of imaging in BSE, to our modelling is logistical. This logistical problem lies in fact that the run-time involved in the reconstruction of the density over the length scales of $\sim 1 \mu\text{m}$, is prohibitive; for an SEM resolution of 10 nm, there are 100 voxels included over $1 \mu\text{m}$, which is 100/15 times the number relevant to the previous illustrations. To circumvent this problem, we work with $\delta=10$ nm which defines the length and width of 20 voxels across the X range of -100 nm to 100 nm. A similar range in Y is

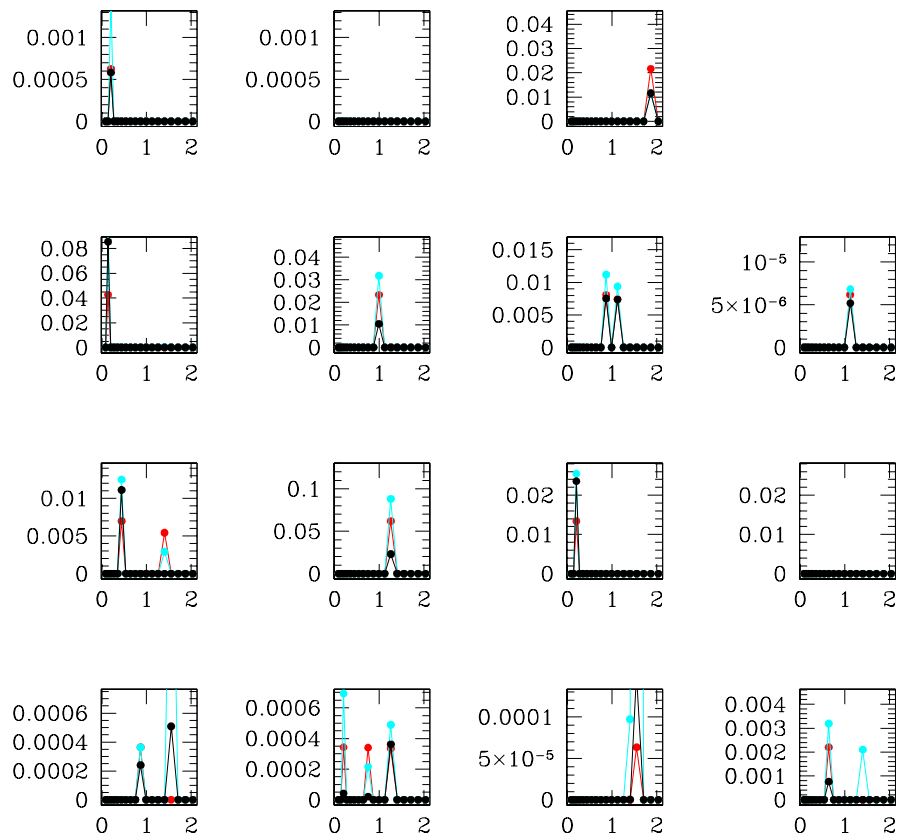


FIG 3. For the simulated Sample II-NiAl, the estimated density $\hat{\rho}(x_i, y_j, z)$ is plotted in model units as a function of Z , at $X = 6.67\mu\text{m}$ distinct values of the locations of the bin along the Y -axis, in the range of $-10\mu\text{m}$ to $10\mu\text{m}$, at intervals of $1.33\mu\text{m}$ from the panel in the lower left-hand corner to the uppermost panel in each figure. The true variation of the learnt material density with Z , is shown in red in each panel, while the material density estimated at the lower and upper bounds of the 95% HPD credible region are shown in cyan and black respectively (in model units). The semi-parametric model for $\Phi(z)$ was used.

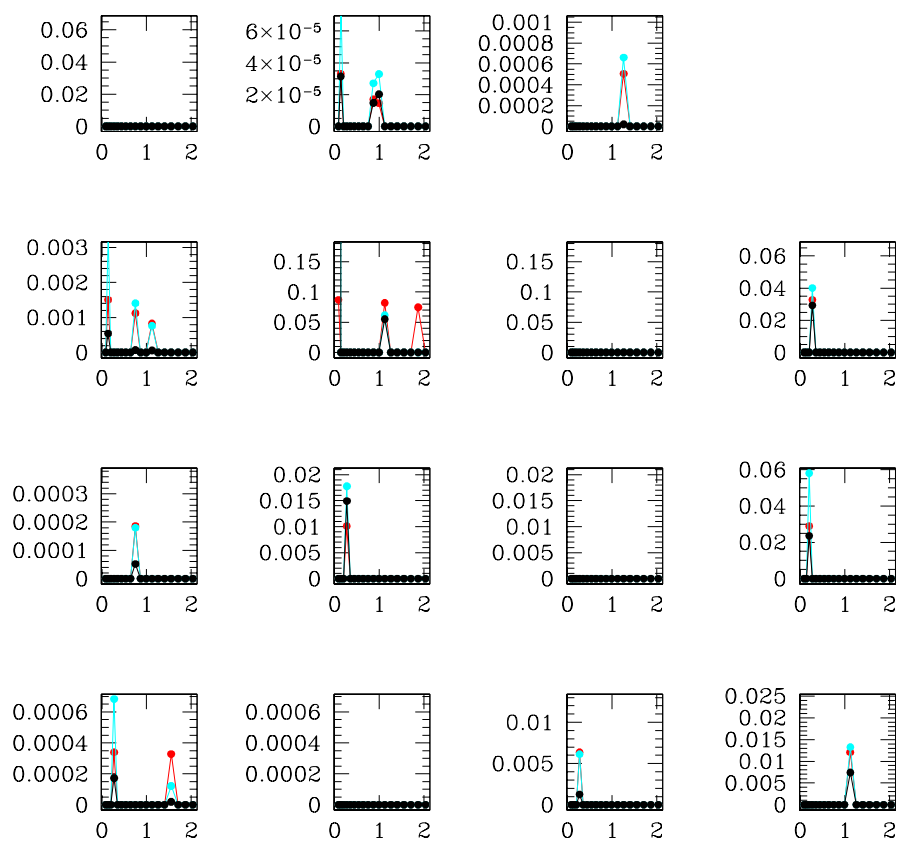


FIG 4. As in Figure 3 except here $\hat{\rho}(x_i, y_j, z)$ is plotted in model units as a function of Z for $X = -6.67\mu\text{m}$, with Y scanning over $y=-10\mu\text{m}$ to $Y=10\mu\text{m}$, at intervals of $1.33\mu\text{m}$ (panel in the lower left-hand corner to the uppermost panel in each figure).

considered. The simulated system is imaged at 10 energy values $\epsilon_k = 10 + 2$ in kV. The atomic numbers of the material used implies that the maximal extent of the interaction-volume is about 590 nm, i.e. all the studied voxels live inside the interaction-volume.

The plots of the learnt density structure for the intrinsically dense and sparse true density functions is shown as a function of Z , for all X and Y , in Fig 5, which display results of runs done with the semi-parametric model for the correction function, at $\sigma_i^{(k)} = 0.05\bar{I}_i^{(k)}$, $i = 1, \dots, N_{data}$, $k = 1, \dots, N_{eng}$. The multi-scale structure of the heterogeneity in these simulated density functions is brought out by presenting the logarithms of the estimated densities alongside $\log \hat{\rho}(\mathbf{x})$.

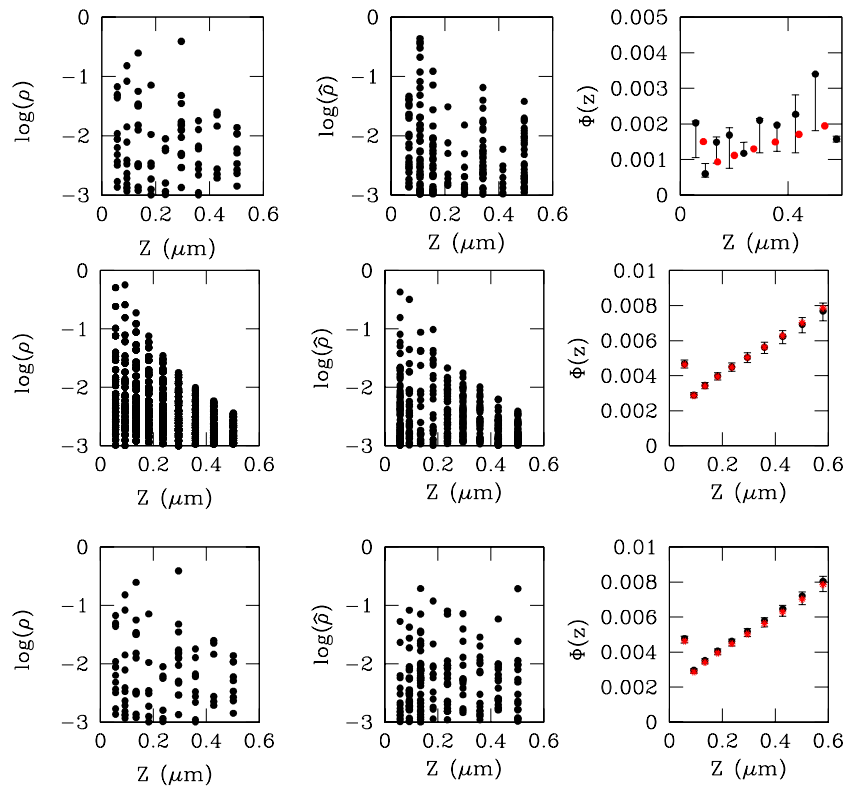


FIG 5. Top row: results of inversion of simulated image data of Sample II-NiAl when a fully non-parametric model for the correction function is used. The true material density structure is presented in the panels on the left, as a function of Z , for all X, Y , in model units. The learnt material density, at the modal level of the posterior, is similarly presented in the middle panels while the learnt function $\Phi(z)$ - the local integral over $\eta(z)$ - is shown as a function of Z in the right panels, in model units. Middle row: the intrinsically dense, true and learnt (at the posterior mode) material density of simulated sample Sample I-NiAl in the left and middle panels respectively with the learnt $\Phi(z)$. A semi-parametric model for the correction function is employed. Bottom row: results from implementing simulated images of Sample II-NiAl when a semi-parametric model for the correction function is employed.

REFERENCES

- DSouza, N., Beanland, R., Hayward, C., & Dong, H. (2011), "Accuracy of composition measurement using X-ray spectroscopy in precipitate-strengthened alloys: Application to Ni-base superalloys," *Acta Materialia*, 59, 1003.

Haario, H., Laine, M., Mira, A., & Saksman, E. (2006), "DRAM: Efficient adaptive MCMC," *Statistics and Computing*, 16, 339.